

Joint unmixing and deconvolution for angular and spectral differential imaging

Olivier Flasseur, Loïc Denis, Éric Thiébaud and Maud Langlois

Abstract—Angular and spectral differential imaging is an observational technique used in astronomy to study the close environment of stars. The relative angular motion and spectral scaling between on-axis and off-axis sources are exploited by processing techniques to separate two components: the residual light from the star and the light coming from surrounding objects such as circumstellar disks. This paper describes a method to unmix these two components and deconvolve the image of disks. It is based on a statistical modeling of the residual star light, in particular its spatial and spectral correlations. These correlations have so far been neglected by standard reconstruction techniques. We show on several datasets from the SPHERE instrument at the Very Large Telescope, Chile, that accounting for correlations strongly improves the reconstructions.

Index Terms—Inverse problems, unmixing, deconvolution, Gaussian scale mixture, covariance matrix.

I. INTRODUCTION

OUR understanding of the formation and evolution of planetary systems has radically evolved these last two decades thanks to unprecedented progress in observational techniques. In particular, several methods have emerged to detect exoplanets [1]. Most of them are classified as *indirect* observational methods since the detections comes from the analysis of perturbations of the host star induced by the presence of the exoplanets. In contrast, *direct imaging* performs the observation and collects photons of both the star and its close environment. This latter observational technique offers the unique capability of acquiring multi-spectral images of the so-called *circumstellar environment* in the vicinity of young stars. Objects of high astrophysical interest located in the circumstellar environment include exoplanets and circumstellar disks made of gas and dust in which exoplanets can form by accretion. In this context, direct imaging is a method of choice to study the interactions between exoplanets and the associated circumstellar disks, as well as the planet formation processes.

Direct imaging requires to face two observational challenges: the objects of interest (disks and exoplanets) have a very low contrast with respect to their host star (typically

lower than $10^{-4} - 10^{-3}$ in the infrared) and are located in the immediate surrounding of the star, which requires a high angular resolution to separate them (disks are generally seen inside an angle of less than 1 arcsecond). The angular resolution requirement can be achieved using large ground-based telescopes equipped with a high-performance adaptive optics system (to compensate in real-time for atmospheric turbulence). The contrast is improved by masking out most of the star light with a coronagraph. However, this is not sufficient to recover interpretable images of the circumstellar environment: residual light from the star still dominates, see Fig. 1. In order to further reduce the impact of the star light, differential imaging is used: several images are captured in configurations that induce a relative motion of the objects of interest with respect to the structures due to the star light (namely, the *speckles* created by the residual phase aberrations in the pupil of the telescope). Two configurations can be used: in angular differential imaging (ADI) [2], a sequence of images is acquired during a few hours of observation. During the acquisition, the pupil of the telescope keeps a constant orientation (so-called *pupil-tracking mode*) while the field-of-view rotates due to Earth's rotation. This leads to a rotation of the objects of interest about the optical axis in the images, with quasi-static speckle created by uncorrected optical aberrations. In spectral differential imaging (SDI) [3], images in several spectral bands are captured. Due to diffraction, the speckle pattern scales linearly with the wavelength, in first approximation. After proper spectral rescaling of the images, the speckle patterns are aligned while the objects of interest undergo a radial motion due to the scaling transform. ADI and SDI can be associated to form Angular and Spectral Differential Imaging (ASDI) sequences. The images recorded in ADI, SDI, or ASDI should be combined, in a processing step, to improve the contrast and to obtain interpretable images of the circumstellar environment. The classical processing pipeline performs first an estimation of the component due to the star (e.g., by averaging the stack of images with aligned speckles), a removal of this component from the data, and finally an alignment and stacking of the residuals (so as to compensate for the rotations and scaling of the field-of-view).

Beyond a simple average, the component due to the star can be estimated using a median (cADI method [2]), a weighted linear combination [4]–[6], or a principal component analysis [7], [8]. However, these approaches suffer from a common pitfall: part of the signal of interest is included in the star component, it is then lost when the star component is subtracted from the data, a phenomenon described as the *self-subtraction problem* [9], [10]. It is particularly important

O. Flasseur is with LESIA, Observatoire de Paris, Université PSL, CNRS, Sorbonne Université, Univ. Paris Diderot, Sorbonne Paris Cité, 5 Place Jules Janssen, 92195 Meudon, France and was previously at Université de Lyon, Université Lyon1, ENS de Lyon, CNRS, Centre de Recherche Astrophysique de Lyon UMR 5574, F-69230, Saint-Genis-Laval, France where most of this work was performed.

L. Denis is with Université de Lyon, UJM-Saint-Etienne, CNRS, Institut d'Optique Graduate School, Laboratoire Hubert Curien UMR 5516, F-42023, Saint-Étienne, France.

É. Thiébaud and M. Langlois are with Université de Lyon, Université Lyon1, ENS de Lyon, CNRS, Centre de Recherche Astrophysique de Lyon UMR 5574, F-69230, Saint-Genis-Laval, France.

close to the star, where the rotations and scalings have the least effect, and the disentangling between the component of interest and the star light is the most difficult. Other artifacts can also be observed: partial replicas, suppression of some smooth extended-structures, smearing or non-uniform attenuations.

To reduce the impact of self-subtraction, several approaches were considered. Some works consider a parametric model of a disk and iteratively adjust its parameters [9], [11]. This kind of approach is only applicable to simple disk structures such as ellipses. Another technique, called Reference Differential Imaging (RDI), uses additional images of an isolated star (i.e., without any exoplanet or disk) either captured simultaneously (the so-called *star-hopping* technique [12]) or from previous observations. The effectiveness of this approach depends on the similarity between the reference and the actual observations (similar star brightness and spectrum, close observation conditions). Finally, the most recent and promising approaches address jointly the problem of estimating the star light residuals and reconstructing the spatial distribution of the disk and exoplanets. In ADI, two approaches based on an inverse problems formulation were recently proposed: MAYONNAISE [13] and REXPACO [14]. These two algorithms use different strategies for the separation of the two components and the regularization of the inversion. MAYONNAISE uses a first step to identify a low-dimension subspace that contains the residual star light (after speckle alignment, the sequence of images is indeed highly correlated). A truncated singular value decomposition (SVD) is applied to the sequence with aligned speckles to estimate the star component, then the residuals are derotated (to align the disk and exoplanet component) and averaged to produce an estimate of the component of interest. The estimation of each component is then alternately refined. The rank of the truncated SVD is progressively increased from 1 to 10. At the end of this first step, the subspace spanned by the sequence of residual star light images is identified. In a second step, several components are estimated by joint minimization of a data fidelity term: the star light residuals (restricted to lie within the subspace identified in the first step), the disk (restricted to have a sparse representation in a wavelet basis), the exoplanets (restricted to be sparse). Positivity constraints are also enforced during the minimization. REXPACO follows quite a different modeling: instead of explicitly estimating the residual star light in each image of the sequence, it builds a statistical model of all fluctuations other than the component of interest (i.e., noise and star light). It learns the spatial correlations of these fluctuations at the scale of 2D image patches, following an approach first introduced for the detection of exoplanets (the so-called PACO algorithm, based on PATCH COvariances [15]). The component of interest is deconvolved with an edge-preserving smoothness regularization and positivity constraint.

This paper addresses the problem of reconstructing circumstellar disks from ASDI sequences. Compared to ADI sequences, this raises several challenges:

- the modeling of temporal and spectral fluctuations of the residual star light,
- the joint exploitation of both spectral and temporal information to effectively extract the component of interest,

- the tractability of estimating high-dimensional models from large datasets.

Typical ASDI datasets produced by the Integral Field Spectrograph (IFS) of the Spectro-Polarimetry High-contrast Exoplanet Research instrument (SPHERE [16]) at the Very Large Telescope (VLT), in Chile, are $N = 290 \times 290$ pixels, have $L = 39$ spectral bands, and $T \approx 100$ exposures. Several hundred million pixel measurements must then be combined to produce a multi-spectral reconstruction of the component of interest.

Our contributions: This paper extends the REXPACO algorithm [14] to ASDI sequences. This extension involves several specific developments, in particular:

- a separable model of the spatial, temporal and spectral covariances,
- a technique to estimate the components of the covariance model,
- a strategy to jointly refine the model of the residual star light and to reconstruct the disk,
- a spatio-spectral regularization of the reconstructed multi-spectral images.

While the observation model is quite specific to direct imaging in astronomy, our statistical modeling of the nuisance terms is very general and could be applied to other imaging modalities for component unmixing problems.

Section II develops the statistical model for the residual star light and different noise contributions. Around this model, section III builds a reconstruction method that extracts and deconvolves the component of interest: the multi-spectral image of the disk that surrounds the star. Results on several ASDI sequences obtained by the SPHERE-IFS instrument at the VLT are presented in section IV.

II. STATISTICAL MODEL OF ALL NUISANCE TERMS

In contrast to other methods in the literature [2], [10], [13], we do not explicitly extract the residual star light component from the data but rather develop a statistical model to capture both the residual star light (i.e., the speckles) and the various noise contributions (photon noise, electronic noise, sensor deficiencies). Thanks to the speckle alignment techniques (namely, pupil tracking and image rescaling according to the wavelength), residual star light is very similar from one image to the next (up to some chromatic factor). There are, however, some fluctuations due to noise, chromatic phenomena, and the evolution of the phase aberrations during observation. These fluctuations display some spatial and spectral correlations and are highly non-stationary: in particular, they are much stronger close to the star (i.e., the image center).

Figure 1 shows an ASDI dataset of a star (SAO 206462) surrounded by a bright disk. Slices along different dimensions of this 4D dataset are displayed. The coronagraphic mask is aligned with the star, at the center of the field-of-view (center of the images shown in Fig.1(a)). Residual star light dominates the central area and extends over most of the field of view. It takes the form of granular intensity structures (speckles). During a pre-processing step, all images were rescaled by a wavelength-specific factor $\lambda_{\text{ref}}/\lambda$ to compensate for diffraction

Time series of multispectral high-contrast observations

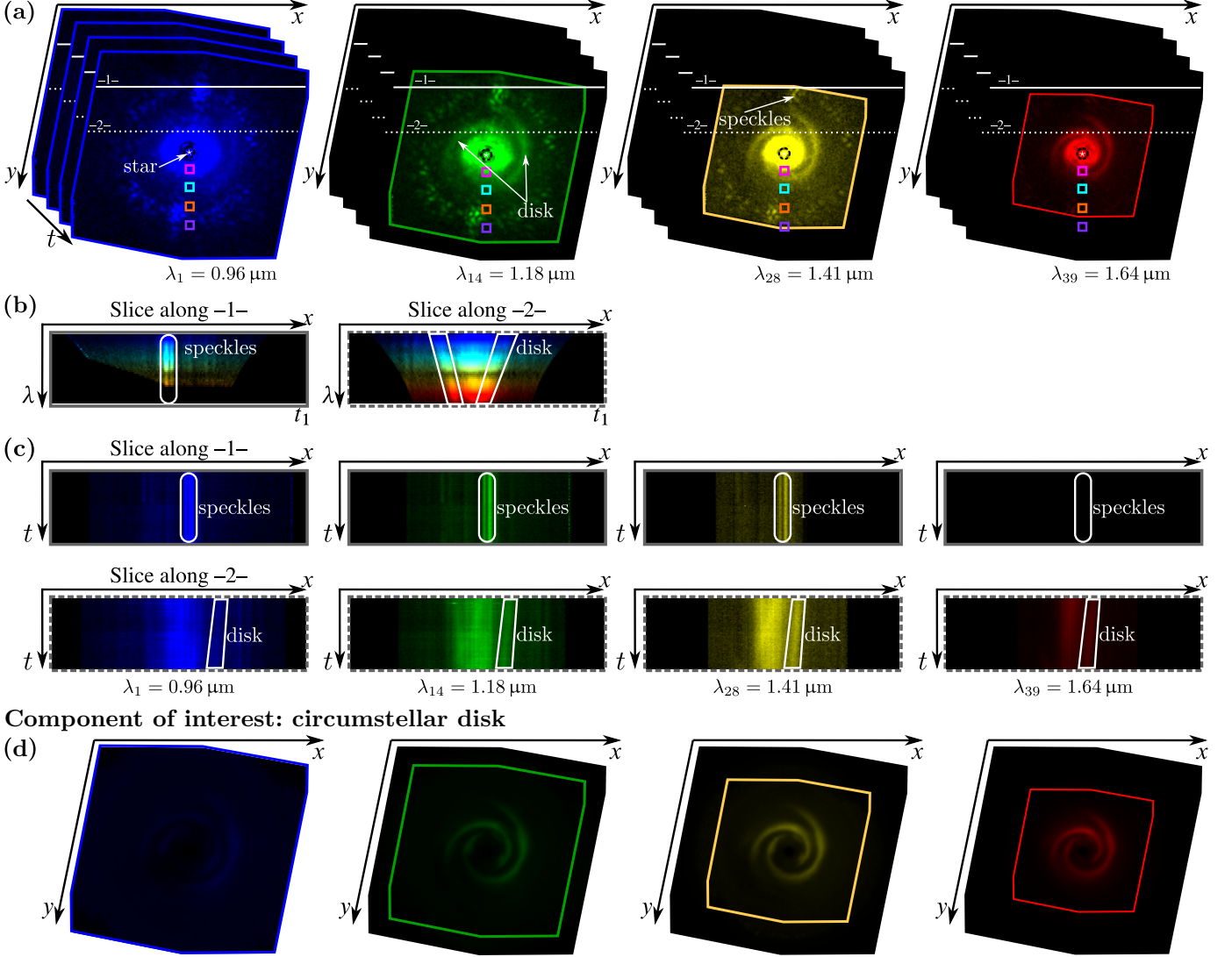


Fig. 1. Illustration of an ASDI dataset: a sequence of multi-spectral cubes of the star SAO 206462 collected by SPHERE-IFS at the VLT, Chile. (a) images captured at different wavelengths; (b) spatio-spectral slices along the two lines -1- and -2- drawn in (a); (c) spatio-temporal slices along the lines -1- and -2-. The four square areas define four regions studied in more details in Fig.2. The component of interest, a spiral-shaped circumstellar disk, is shown in (d) based on our reconstruction given in Fig.6. In the first channel, shown in blue, the signal of the disk is faint compared to the stellar leakages.

and spatially align the speckles. The solid line -1- drawn in the x direction in Fig.1(a) crosses a bright speckle. This speckle is visible in the left part of Fig.1(b) and the first row of Fig.1(c). It remains at the same spatial location for all wavelengths λ and all capture times t . Structures of interest, such as the disk that surrounds the star SAO 206462, undergo a rotation about the image center throughout time and a scaling with the wavelength (due to the rescaling applied in the preprocessing step). These spatial transformations are visible in the slices along the dotted line -2- drawn in the images of Fig.1(a): the line crosses the disk (as well as an area with strong residual star light, close to the image center). The spatio-spectral slice shown at the right of Fig.1(b) displays a scaling of the disk with respect to the wavelength (shorter wavelengths are dilated due to the speckle-aligning preprocessing), whereas the rotation motion can be noted in the spatio-temporal slices shown at the bottom of Fig.1(c),

in particular for a bright structure of the disk put in a box, which is moving closer to the image center during the sequence. Fig.1(d) shows only the component of interest: the circumstellar disk. The images were obtained with the reconstruction method introduced in this paper, see Fig.6 for a different visualization of the reconstructed disk. By comparing Fig.1(a) and Fig.1(d), it appears that high-contrast observations suffer from a strong nuisance component which has to be numerically suppressed in order to reconstruct the component of interest.

The modeling of residual star light and noise has a strong impact on the reconstruction of the component of interest u , as discussed in section IV. In the following of the section, we assume that the object u has a negligible impact on the statistical distribution of the nuisance term, i.e., the statistical distribution of the aligned data $p_V(v)$ in the absence of disk or exoplanet is identical to the distribution of the residuals

$p_V(\mathbf{v} - \mathbf{M}\mathbf{u})$ obtained when the modeled contribution $\mathbf{M}\mathbf{u}$ of the component of interest has been subtracted from the data (the direct model, \mathbf{M} , is presented in section III-A, Eq.(23)). This assumption is reasonable in high contrast imaging since residual light from the star is the dominant component in the data: the photon noise level is then almost independent of the presence of other sources in the field of view. Besides, we introduce in section III-C a strategy to jointly estimate the statistical distribution of the nuisance terms and reconstruct the component of interest. This strategy extends the applicability of our modeling to data with signal-dependent perturbations.

A. Patch-based statistical modeling

Image patches (i.e., neighborhoods of a few tens to a hundred pixels) offer an interesting trade-off between locality (small enough to capture a local behavior) and complexity (they include enough pixels to collect geometrical and textural information). Their use has been very successful in image restoration, from methods based on image self-similarity [17], collaborative filtering [18], sparse coding [19], [20], mixture models [21], [22], or Gaussian models [23]. Whereas deep neural networks have become the state-of-the-art approach to learn rich models of natural images (either generative or discriminative), patch-based models retain serious advantages when the number of training samples is limited or in the case of highly non-stationary images. As can be seen in Fig.1(a), images in an ASDI dataset are far from stationary. Observations made during separate nights around different stars also often display significantly different structures because of changes in the observing conditions (which impact the residual aberrations uncorrected by adaptive optics, and hence the spatial distribution of speckles due to star light) and star brightness. This limits the possibility to use external observations to learn a model to process a specific ASDI sequence and motivates the development of a patch-based approach based solely on the ASDI sequence of interest.

Under our patch-based model, the distribution of an ASDI sequence $\mathbf{v} \in \mathbb{R}^{NLT}$ *without disk or exoplanet* (formed by the collection of T multi-spectral images with L spectral bands and N pixels in each band) is given by:

$$p_V(\mathbf{v}) \approx \prod_{n \in \mathbb{K}} p_{V_n}(\mathbf{E}_n \mathbf{v}), \quad (1)$$

where p_V is the joint distribution of the whole ASDI dataset, \mathbf{E}_n is the linear operator that extracts a $K \times L \times T$ -pixel spatio-spectro-temporal patch centered at the n -th spatial location of the field-of-view (i.e., $\mathbf{v}_n = \mathbf{E}_n \mathbf{v}$ is a 4D-patch, we do not differentiate the x and y spatial dimensions to simplify the notations but rather use 2D spatial indices n). The set of spatial locations \mathbb{K} is defined to prevent patch overlapping while tiling the whole field-of-view (i.e., $\text{Card}(\mathbb{K}) \times K = N$ and juxtaposed square patches are used).

The model (1) assumes a statistical independence between patches, which is a simplifying hypothesis that eases a data-driven learning of the distribution p_V . In the sequel, each distribution p_{V_n} is modeled by a different multivariate Gaussian in order to capture the correlations between observations

within a spatio-spectro-temporal patch. By adapting the parameters of these Gaussian distributions to the spatial location n , a non-stationary model is obtained, with the capability to capture the variations between areas close to the star (at the center of the image) and areas farther away. The statistical model of a patch is thus given by:

$$p_{V_n}(\mathbf{v}_n) = \frac{1}{\sqrt{|2\pi\mathbf{C}_n|}} \exp\left(-\frac{1}{2}\|\mathbf{v}_n - \boldsymbol{\mu}_n\|_{\mathbf{C}_n^{-1}}^2\right), \quad (2)$$

with $\|\mathbf{a}\|_{\mathbf{B}}^2 = \mathbf{a}^\top \mathbf{B} \mathbf{a}$ and $|\mathbf{C}_n|$ the determinant of matrix \mathbf{C}_n . The Gaussian distribution p_{V_n} is parameterized by the mean patch $\boldsymbol{\mu}_n \in \mathbb{R}^{KLT}$ and the covariance matrix $\mathbf{C}_n \in \mathbb{R}^{KLT \times KLT}$. In order to estimate these two quantities at each location n , additional hypotheses and an estimation technique are required.

B. Constraining the structure of the average vector and the covariance matrix

Estimating and handling different Gaussian parameters for each patch location is not doable owing to the number of parameters involved: the set of all mean vectors $\{\boldsymbol{\mu}_n\}_{n \in \mathbb{K}}$ has as many free parameters as the total number of measurements in \mathbf{v} (i.e., NLT) and the set of all covariance matrices $\{\mathbf{C}_n\}_{n \in \mathbb{K}}$ represents many times the number of measurements in \mathbf{v} (more precisely, $NLT(KLT + 1)/2$ free parameters, which represents more than 300 000 times the size of \mathbf{v} for typical values of $K \approx 13 \times 13$, $L \approx 39$, and $T \approx 100$).

There are two options to reduce the number of parameters in the Gaussian models of equations (1) and (2): (i) assume some level of stationarity for the means or covariances with respect to the spatial location n ; (ii) enforce a structure on the mean $\boldsymbol{\mu}_n$ and the covariance \mathbf{C}_n to limit the number of free parameters. Beyond obtaining more tractable models, these assumptions are also indispensable, for a single ASDI dataset \mathbf{v} , to constrain the estimator of the parameters of the Gaussian models.

The strong spatial non-stationarity of ASDI datasets led us to favor option (ii). We considered several ways to select a structure suitable to ASDI observations and built on our experience of point-source detection in ASDI datasets (i.e., exoplanet detection [15], [24], [25]). We found that it is preferable to use a common mean vector $\boldsymbol{\mu}_n$ for all times t rather than a time-specific mean vector common to all wavelengths (the spectral variations being stronger than the temporal fluctuations):

$$\boldsymbol{\mu}_n = \text{vec} \left(\left(\begin{array}{c} | \\ \boldsymbol{\mu}_n^{\text{spec}} \\ | \end{array} \right) \left(\overset{\leftarrow T \rightarrow}{1 \quad \cdots \quad 1} \right) \right), \quad (3)$$

where $\text{vec}(\cdot)$ performs the vectorization of a matrix by stacking its columns (it transforms a $KL \times T$ matrix into a vector of dimension KLT) and $\boldsymbol{\mu}_n^{\text{spec}}$ is a KL -pixel multi-spectral vector that represents the temporal average of the multi-spectral patches.

To capture the structures of both the spatial and the spectral covariances, we model the covariance between two pixels of the patch \mathbf{v}_n by:

$$\begin{aligned} \text{Cov}[\mathbf{v}_{n,(k_1,\ell_1,t_1)}, \mathbf{v}_{n,(k_2,\ell_2,t_2)}] &= 0 \text{ if } t_1 \neq t_2, \\ &= \sigma_{n,t}^2 \mathbf{C}_n^{\text{spat}}(k_1, k_2) \mathbf{C}_n^{\text{spec}}(\ell_1, \ell_2) \text{ if } t_1 = t_2 = t, \end{aligned} \quad (4)$$

where $\sigma_{n,t}^2$ is a scalar that encodes the global level of fluctuation in the multi-spectral slice at time t , $\mathbf{C}_n^{\text{spat}}$ is a $K \times K$ covariance matrix encoding the spatial structure of the fluctuations (a K -pixel spatial patch corresponds to a 2D square window, so this covariance matrix contains information about 2D spatial structures), and matrix $\mathbf{C}_n^{\text{spec}}$ is an $L \times L$ covariance matrix encoding spectral correlations. To prevent a degeneracy by multiplicative factors, we normalize covariance matrices $\mathbf{C}_n^{\text{spat}}$ and $\mathbf{C}_n^{\text{spec}}$ such that their trace be equal to K and L , respectively. In the covariance model of equation (4), multi-spectral slices at different times t_1 and t_2 are considered uncorrelated (and, thus, independent given the joint Gaussian assumption of equation (2)). The time-varying variance parameter $\sigma_{n,t}^2$ plays the role of a scale parameter in a compound-Gaussian model [26] (also known as a Gaussian scale mixture model, see e.g. [27]). A large value of parameter $\sigma_{n,t}^2$ almost discards the time frame t from the n -th 4D patch, which limits the impact of possible outliers [28].

The covariance structure given in equation (4) corresponds to the following separable covariance matrix:

$$\text{Cov}[\mathbf{v}_n] = \text{diag}(\sigma_n^2) \otimes \mathbf{C}_n^{\text{spec}} \otimes \mathbf{C}_n^{\text{spat}}, \quad (5)$$

where $\text{diag}(\sigma_n^2)$ is a $T \times T$ diagonal matrix whose t -th diagonal entry is $\sigma_{n,t}^2$ and \otimes is Kronecker matrix product: $\mathbf{A} \otimes \mathbf{B}$, with $\mathbf{A} \in \mathbb{R}^{n \times n}$ and $\mathbf{B} \in \mathbb{R}^{m \times m}$, is the $nm \times nm$ matrix with a $n \times n$ block structure such that the ij -th block is the $m \times m$ matrix $A_{ij}\mathbf{B}$. Note that this is equivalent to modeling each multi-spectral slice $\mathbf{v}_{n,t} \in \mathbb{R}^{KL}$ of \mathbf{v}_n as random vectors following the compound-Gaussian model $\mathcal{N}(\boldsymbol{\mu}_n^{\text{spec}}, \sigma_{n,t}^2 \mathbf{C}_n^{\text{spec}} \otimes \mathbf{C}_n^{\text{spat}})$, or that the scaled and centered vectors $\frac{1}{\sigma_{n,t}}(\mathbf{v}_{n,t} - \boldsymbol{\mu}_n^{\text{spec}})$ are independent and identically distributed for all $1 \leq t \leq T$ according to the centered Gaussian $\mathcal{N}(\mathbf{0}, \mathbf{C}_n^{\text{spec}} \otimes \mathbf{C}_n^{\text{spat}})$.

With the structure of the mean vector $\boldsymbol{\mu}_n$ given in equation (3), corresponding to a multi-spectral patch constant through time, there are only NL free parameters to estimate all mean vectors from $\mathbf{v} \in \mathbb{R}^{NLT}$. The covariance structure defined in equations (4) and (5) leads to $T + K(K+1)/2 + L(L+1)/2 - 2$ free parameters per 4D patch (the -2 comes from the two normalization constraints), which leads to approximately $NK/2$ free parameters for the whole ASDI dataset (because $K \gg L$), and is typically one to two orders of magnitudes smaller than the total number of measurements in \mathbf{v} ($K/2$ is typically less than one hundred whereas LT is several thousands). Jointly with an adequate estimation method, the structures assumed in equations (3), (4), and (5) can thus be used to derive a *non-stationary* model of the nuisance terms.

C. Estimation of the model parameters $\boldsymbol{\mu}_n$ and \mathbf{C}_n

The estimation of the parameters of a separable covariance model has been studied by several previous works, see for

example [29]–[31]. We build on these works and introduce several additional elements: (i) whereas most works consider decompositions of the covariance matrix as a Kronecker product of two factors, we also include in equations (4) and (5) the temporal scaling factors $\sigma_{n,t}$ for increased robustness [28]; (ii) given the limited number of samples, we replace maximum likelihood estimates by shrinkage covariance estimators [32], [33] to ensure that all estimated covariance matrices are definite positive and to reduce estimation errors; (iii) to account for the superimposition of a component of interest and nuisance terms, we develop a joint estimation strategy in section III-C based on the estimation technique developed in this paragraph.

We first derive the maximum likelihood estimates (MLEs) of the means $\boldsymbol{\mu}_n^{\text{spec}}$, variance factors $\sigma_{n,t}^2$ and matrices $\mathbf{C}_n^{\text{spec}}$ and $\mathbf{C}_n^{\text{spat}}$:

Proposition 1 (Maximum Likelihood Parameter Estimates). *The maximum likelihood estimates, under the Gaussian model of section II-B are:*

$$\hat{\boldsymbol{\mu}}_n^{\text{spec}} = \left(\sum_{t=1}^T \hat{\sigma}_{n,t}^{-2} \mathbf{v}_{n,t} \right) / \left(\sum_{t=1}^T \hat{\sigma}_{n,t}^{-2} \right) \quad (6)$$

$$\hat{\sigma}_{n,t}^2 = \frac{1}{KL} \|\mathbf{v}_{n,t} - \hat{\boldsymbol{\mu}}_n^{\text{spec}}\|_{\hat{\mathbf{C}}_n^{\text{spec}-1} \otimes \hat{\mathbf{C}}_n^{\text{spat}-1}}^2 \quad (7)$$

$$\hat{\mathbf{C}}_n^{\text{spec}} = \frac{1}{TK} \sum_{t=1}^T \frac{1}{\hat{\sigma}_{n,t}^2} \bar{\mathbf{V}}_t^\top \hat{\mathbf{C}}_n^{\text{spat}-1} \bar{\mathbf{V}}_t \quad (8)$$

$$\hat{\mathbf{C}}_n^{\text{spat}} = \frac{1}{TL} \sum_{t=1}^T \frac{1}{\hat{\sigma}_{n,t}^2} \bar{\mathbf{V}}_t \hat{\mathbf{C}}_n^{\text{spec}-1} \bar{\mathbf{V}}_t^\top, \quad (9)$$

where $\bar{\mathbf{V}}_t$ is a $K \times L$ matrix corresponding to the centered multi-spectral patch at time t : at row k and column ℓ it is equal to $[\mathbf{v}_{n,t}]_{k,\ell} - [\boldsymbol{\mu}_n^{\text{spec}}]_{k,\ell}$.

Proof. See appendix A. \square

The multi-spectral mean $\hat{\boldsymbol{\mu}}_n^{\text{spec}}$ is obtained by weighted averaging, with weights inversely proportional to the variance $\sigma_{n,t}^2$: this limits the impact of outliers. The variance $\sigma_{n,t}^2$ corresponds to the average squared deviation to the mean, computed after proper spatial and spectral whitening. By factoring matrices $\hat{\mathbf{C}}_n^{\text{spat}-1}$ and $\hat{\mathbf{C}}_n^{\text{spec}-1}$ under the form $\mathbb{W}_n^{\text{spat}} \mathbb{W}_n^{\text{spat}\top}$ and $\mathbb{W}_n^{\text{spec}} \mathbb{W}_n^{\text{spec}\top}$ (for example by Cholesky factorization), products of the form $\mathbb{W}_n^{\text{spat}\top} \bar{\mathbf{V}}_t$ can be interpreted as a spatial whitening operation applied to each column of the centered multi-spectral patch $\bar{\mathbf{V}}_t$, and products of the form $\mathbb{W}_n^{\text{spec}\top} \bar{\mathbf{V}}_t^\top$ can be interpreted as a spectral whitening applied to each row of $\bar{\mathbf{V}}_t$. Spectral and spatial covariance matrices $\hat{\mathbf{C}}_n^{\text{spec}}$ and $\hat{\mathbf{C}}_n^{\text{spat}}$ are thus estimated by forming the covariance of spatially (resp. spectrally) whitened vectors, with weights inversely proportional to the variance $\sigma_{n,t}^2$.

From the expressions in Proposition 1, it is not possible to derive a closed-form expression of each parameter that does not depend on other parameters. Yet, these formulae can be applied alternately until convergence, a method called *flip-flop* in [29] where a faster convergence is reported compared to maximizing the log-likelihood using an iterative optimization algorithm (Newton's method).

Figure 2 illustrates the spatial and spectral covariance matrices estimated from an ASDI dataset captured at the VLT, in

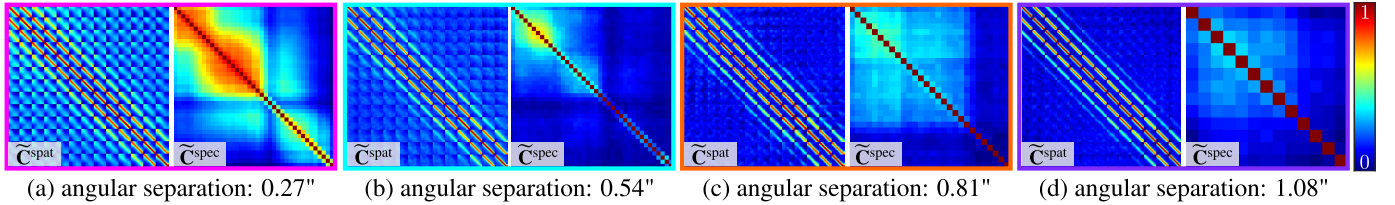


Fig. 2. Spatial and spectral correlation matrices computed in the four regions depicted in Fig.1(a). The angular separation with respect to the star (i.e., image center) increases from the region in (a), close to the star, to the region in (d), which is farther.

Chile. These matrices are computed from patches extracted at the center of the four regions of the field of view indicated by color boxes in Fig.1(a). To compare matrices with very different variances, we normalized each covariance $\text{Cov}[a,b]$ by $\sqrt{\text{Cov}[a,a]\text{Cov}[b,b]}$, i.e., we show the correlation coefficients. Due to the vectorization of 2D spatial patches, the spatial correlations display a blocky structure. The spatial correlations within a patch globally decrease with the 2D distance between pixels. They are stronger in the area (a) which is the closest to the star. Spectral correlations are also much stronger close to the star. As can be observed in Fig.1(a), after the scaling transform applied in the pre-processing step, regions far from the star are not seen at the longest wavelengths. The size of multi-spectral patches extracted in these regions is reduced from KL to KL_{eff} pixels (with $L_{\text{eff}} < L$ the effective number of wavelengths seen at location n) and the size of the spectral covariance matrix $\hat{\mathbf{C}}_n^{\text{spec}}$ is reduced accordingly, from $L \times L$ to $L_{\text{eff}} \times L_{\text{eff}}$.

To reduce the estimation error on the covariance matrices and ensure their definite-positiveness, shrinkage techniques combine the maximum likelihood estimator with another estimator of smaller variance. Like in our previous works [14], [15], [25], we consider the convex combination between the sample covariance and a diagonal covariance, with a non-constant diagonal. This corresponds to shrinking off-diagonal entries of the covariance matrix by a factor $1 - \tilde{\rho}$, where $\tilde{\rho}$ is estimated from the data, see [15], [32], [33]. We recall in the following Proposition the general expression of a shrinkage covariance estimator:

Proposition 2 (Shrinkage Estimator of Covariance).

Let $\{\mathbf{v}_{n,t}\}_{t=1..T}$ be a collection of T independent random vectors, such that $(\mathbf{v}_{n,t} - \boldsymbol{\mu}_n) / \sigma_{n,t}$ be i.i.d. for all t according to a Gaussian distribution $\mathcal{N}(\mathbf{0}, \mathbf{C}_n)$. The bias-variance trade-off is improved by replacing the maximum likelihood covariance estimator:

$$\hat{\mathbf{C}}_n = \frac{1}{T} \sum_{t=1}^T \frac{1}{\sigma_{n,t}^2} (\mathbf{v}_{n,t} - \boldsymbol{\mu}_n)(\mathbf{v}_{n,t} - \boldsymbol{\mu}_n)^\top, \quad (10)$$

by the shrinkage estimator:

$$\tilde{\mathbf{C}}_n = (1 - \tilde{\rho}_n) \hat{\mathbf{C}}_n + \tilde{\rho}_n \text{Diag}(\hat{\mathbf{C}}_n), \quad (11)$$

with $\text{Diag}(\mathbf{C})$ the diagonal matrix such that $[\text{Diag}(\mathbf{C})]_{i,i} = [\mathbf{C}]_{i,i}$ and $\tilde{\rho}_n \in [0, 1]$. Parameter $\tilde{\rho}_n$ controls the level of shrinkage applied to off-diagonal values of $\hat{\mathbf{C}}_n$. The data-

driven value for parameter $\tilde{\rho}_n = \rho(\hat{\mathbf{C}}_n; \tilde{T}_n)$ given by the oracle-approximating method of Chen et al [33] is:

$$\rho(\mathbf{C}; T) = \frac{\text{tr}(\mathbf{C}^2) + \text{tr}^2(\mathbf{C}) - 2 \text{tr}[\text{Diag}(\mathbf{C})^2]}{(T + 1)(\text{tr}(\mathbf{C}^2) - \text{tr}[\text{Diag}(\mathbf{C})^2])}, \quad (12)$$

where \tilde{T}_n corresponds to the equivalent number of terms in the weighted sum (10):

$$\tilde{T}_n = \frac{(\sum_t 1/\sigma_{n,t}^2)^2}{\sum_t 1/\sigma_{n,t}^4}. \quad (13)$$

Proof. The derivation of the shrinkage factor is based on [33] and is given in [15], appendix A. The equivalent number of terms was first introduced in [28]. \square

The estimator $\tilde{\mathbf{C}}_n$ defined in Proposition 2 shrinks off-diagonal values of $\hat{\mathbf{C}}_n$ towards 0 (by multiplication by the factor $1 - \tilde{\rho}_n$) and leaves diagonal values unchanged (i.e., the variances). Beyond reducing the estimation error, the shrinkage estimator also ensures that $\tilde{\mathbf{C}}_n$ is positive definite, which is essential in section III since the cost function that is minimized to perform image reconstruction involves the inverse of the covariance matrix. Compared to other covariance matrix regularization strategies such as diagonal loading (i.e., adding a fraction of the identity matrix $\epsilon \mathbf{I}$ to $\hat{\mathbf{C}}_n$), Proposition 2 is attractive because it is data-driven: it adapts to the fluctuations observed in the data and the number of samples. It is thus well-suited to imaging systems suffering from non-stationary perturbations.

To apply Proposition 2, the true mean $\boldsymbol{\mu}_n$ and scale factors $\sigma_{n,t}$ are replaced by their estimates, which requires that the estimation error on these parameters be low. The expression of $\tilde{\mathbf{C}}_n$ is general, it does not include the specific structure of our problem, namely, the spatio-spectral separability. Before specializing the expression of the shrinkage covariance estimator to this structure, we give in Proposition 3 an equivalent definition of the shrinkage estimator.

Proposition 3 (Loss function associated to the shrinkage covariance estimator).

The shrinkage covariance matrix estimator $\tilde{\mathbf{C}}_n$ defined in Proposition 2 is the minimizer of a modified Gaussian col-log-likelihood:

$$\tilde{\mathbf{C}}_n = \arg \min_{\mathbf{C}} \frac{T}{2} \log |\mathbf{C}| + \sum_{t=1}^T \frac{1}{2\sigma_{n,t}^2} \|\mathbf{v}_{n,t} - \boldsymbol{\mu}_n\|_{\mathbf{\Gamma}}^2, \quad (14)$$

with $\mathbf{\Gamma} = \boldsymbol{\Psi}_n \odot (\mathbf{C}^{-1})$ the shrunk precision matrix, defined as the Hadamard (element-wise) product between a weighting

matrix Ψ_n and the precision matrix \mathbf{C}^{-1} . The weighting matrix Ψ_n has 1 on the diagonal and the value $(1 - \tilde{\rho}_n)$ off the diagonal ($\tilde{\rho}_n$ is defined in Prop.2).

Proof. This is a generalization of Eq.(30) in [15], the proof is given in appendix B. \square

Note that the expression of the shrinkage estimator in Eq.(11) can be more compactly written $\tilde{\mathbf{C}}_n = \Psi_n \odot \hat{\mathbf{C}}_n$. Proposition 3 shows how to modify the co-log-likelihood so that the covariance matrix that minimizes the loss function changes from the maximum likelihood estimator $\hat{\mathbf{C}}_n$ to the shrinkage estimator $\tilde{\mathbf{C}}_n$.

Based on Proposition 3, we introduce a loss function suitable for separable covariance matrices:

Proposition 4 (Loss function for separable covariance matrix estimation).

Let us define the loss function \mathcal{D}_n :

$$\mathcal{D}_n(\mathbf{v}_n; \boldsymbol{\mu}_n^{\text{spec}}, \boldsymbol{\sigma}_n, \mathbf{C}_n^{\text{spat}}, \mathbf{C}_n^{\text{spec}}) = \frac{T}{2} \log |\text{diag}(\boldsymbol{\sigma}_n^2) \otimes \mathbf{C}_n^{\text{spec}} \otimes \mathbf{C}_n^{\text{spat}}| + \sum_{t=1}^T \frac{1}{2\sigma_{n,t}^2} \|\mathbf{v}_{n,t} - \boldsymbol{\mu}_n^{\text{spec}}\|_{\Gamma}^2, \quad (15)$$

where $\Gamma = [(\Psi_n^{\text{spec}} \odot \mathbf{C}_n^{\text{spec}}) \otimes (\Psi_n^{\text{spat}} \odot \mathbf{C}_n^{\text{spat}})]^{-1}$ is the shrunk spatio-spectral precision matrix. We define the weighting matrices like in Proposition 3: matrix Ψ_n^{spec} is the $L \times L$ matrix with 1 on the diagonal and the value $(1 - \tilde{\rho}_n^{\text{spec}})$ off-diagonal, and matrix Ψ_n^{spat} is the $K \times K$ matrix with 1 on the diagonal and the off-diagonal value $(1 - \tilde{\rho}_n^{\text{spat}})$. Shrinkage parameters are computed with:

$$\tilde{\rho}_n^{\text{spec}} = \rho(\hat{\mathbf{C}}_n^{\text{spec}}; \tilde{\mathbf{P}}_n^{\text{spec}}), \quad (16)$$

$$\tilde{\rho}_n^{\text{spat}} = \rho(\hat{\mathbf{C}}_n^{\text{spat}}; \tilde{\mathbf{P}}_n^{\text{spat}}), \quad (17)$$

and the equivalent number of terms defined by:

$$\tilde{\mathbf{P}}_n^{\text{spec}} = K \frac{(\sum_t 1/\hat{\sigma}_{n,t}^2)^2}{\sum_t 1/\hat{\sigma}_{n,t}^4} \quad \text{and} \quad \tilde{\mathbf{P}}_n^{\text{spat}} = L \frac{(\sum_t 1/\hat{\sigma}_{n,t}^2)^2}{\sum_t 1/\hat{\sigma}_{n,t}^4}. \quad (18)$$

The set of parameters $\{\hat{\boldsymbol{\mu}}_n^{\text{spec}}, \hat{\boldsymbol{\sigma}}_n^2, \tilde{\mathbf{C}}_n^{\text{spec}}, \tilde{\mathbf{C}}_n^{\text{spat}}\}$ that minimize \mathcal{D}_n , for fixed values of the shrinkage parameters $\tilde{\rho}_n^{\text{spec}}$ and $\tilde{\rho}_n^{\text{spat}}$, verifies the following equations:

$$\hat{\boldsymbol{\mu}}_n^{\text{spec}} = \left(\sum_{t=1}^T \frac{1}{\hat{\sigma}_{n,t}^2} \mathbf{v}_{n,t} \right) / \left(\sum_{t=1}^T \frac{1}{\hat{\sigma}_{n,t}^2} \right) \quad (19)$$

$$\hat{\sigma}_{n,t}^2 = \frac{1}{KL} \|\mathbf{v}_{n,t} - \hat{\boldsymbol{\mu}}_n^{\text{spec}}\|_{\Gamma}^2 \quad (20)$$

$$\tilde{\mathbf{C}}_n^{\text{spec}} = \Psi_n^{\text{spec}} \odot \frac{1}{TK} \sum_{t=1}^T \frac{1}{\hat{\sigma}_{n,t}^2} \bar{\mathbf{V}}_t^{\top} (\Psi_n^{\text{spat}} \odot \tilde{\mathbf{C}}_n^{\text{spat}-1}) \bar{\mathbf{V}}_t \quad (21)$$

$$\tilde{\mathbf{C}}_n^{\text{spat}} = \Psi_n^{\text{spat}} \odot \frac{1}{TL} \sum_{t=1}^T \frac{1}{\hat{\sigma}_{n,t}^2} \bar{\mathbf{V}}_t (\Psi_n^{\text{spec}} \odot \tilde{\mathbf{C}}_n^{\text{spec}-1}) \bar{\mathbf{V}}_t^{\top} \quad (22)$$

where $\bar{\mathbf{V}}_t$ is defined as in Proposition 1.

Proof. See appendix C. \square

The loss function \mathcal{D}_n is a direct application of Proposition 3 to the structured covariance matrix defined in Eq.(5). As in Proposition 1, Eqs.(19)–(22) form a set of non-linear equations that can be applied iteratively until a fixed point is reached.

III. RECONSTRUCTION OF THE COMPONENT OF INTEREST

A. Direct model

We extend the forward model developed for ADI in [14] by including the spectral dimension. Since the whole ASDI sequence is acquired within a short time (a few hours during a single night), the component that contains the circumstellar sources such as the disk and possibly exoplanets *does not evolve* during the observations (rotation of the disk or exoplanets about their host star is negligible at such short time scales). The multi-spectral image of this component is simply described by the vector $\mathbf{u} \in \mathbb{R}_+^{N'L}$ of its pixel values (the number N' of pixels in each spectral band of the reconstruction may differ from N , note that there is no temporal dimension in the reconstruction). The contribution of \mathbf{u} to the data \mathbf{v} is modeled by the linear operator:

$$\mathbf{M}\mathbf{u}, \quad \text{with } \mathbf{M} = \begin{pmatrix} \mathbf{M}_1 \\ \vdots \\ \mathbf{M}_T \end{pmatrix} \quad \text{and } \mathbf{M}_t = \mathbf{S}\mathbf{Z}\mathbf{A}\mathbf{R}_t\mathbf{B}_t, \quad (23)$$

where \mathbf{M}_t , the model for the t -th frame, accounts for several instrumental effects:

- a *blur* \mathbf{B}_t due to the instrumental blurring modeled as a 2D discrete convolution by the off-axis point spread function (PSF),
- a *rotation* \mathbf{R}_t applied to all off-axis sources due to the pupil-tracking mode (the field-of-view rotates while the residual star light remains fixed), implemented as a sparse interpolation matrix,
- an *attenuation* \mathbf{A} , very strong on the optical axis, then quickly decreasing (due to the coronagraph), modeled as a diagonal matrix [14],
- the absence of measurements outside the spatial extension of the sensor (a non-square area due to the instrumental design of the integral field spectrograph), modeled as a diagonal matrix \mathbf{Z} that replaces values outside the sensor area by *zeros* and keeps other values unchanged.
- the image *scaling* applied during the pre-processing step produces a last transform \mathbf{S} (time-invariant), corresponding to a sparse interpolation matrix.

With the SPHERE-IFS instrument, the off-axis point spread function (PSF) is quite stable and its core is almost rotation invariant. The model given in equation (23) can thus be approximated by:

$$\mathbf{M}\mathbf{u} \approx \begin{pmatrix} \mathbf{F}_1 \\ \vdots \\ \mathbf{F}_T \end{pmatrix} \mathbf{B}\mathbf{u}. \quad (24)$$

where \mathbf{B} is a time-invariant blurring operator and $\{\mathbf{F}_t\}_{t=1..T}$ are sparse matrices that perform rotations, scalings, and attenuations according to the transmission of the coronagraph and the sensor field-of-view. The model of equation (24) is

only approximate: it neglects possible anisotropies or temporal evolutions of the PSF. Thanks to this approximation, a single convolution of the multi-spectral cube is performed instead of T convolutions, which leads to a dramatic acceleration of the numerical evaluation of the forward model (by 1 to 2 orders of magnitude) which is critical to achieving reconstructions on datasets in the order of a few hours. We checked that the impact of these approximations on the reconstructions was negligible in practice.

B. Regularized inversion

We reconstruct the component of interest using a penalized maximum likelihood approach, i.e., by solving the following numerical optimization problem:

$$\hat{\mathbf{u}} = \arg \min_{\mathbf{u} \geq 0} -\log p_V(\mathbf{v} | \mathbf{M}\mathbf{u}; \{\boldsymbol{\mu}_n, \mathbf{C}_n\}_{n \in \mathbb{K}}) + \mathcal{R}(\mathbf{u}), \quad (25)$$

where $\mathcal{R}(\mathbf{u})$ is a regularization term to favor plausible reconstructions \mathbf{u} . We selected a combination of two regularization functions: an edge-preserving one that favors smooth images with sharp edges co-located at all wavelengths and a sparsity-inducing L^1 norm. The regularization writes:

$$\mathcal{R}(\mathbf{u}) = \beta_{\text{smooth}} \sum_{n=1}^{N'} \sqrt{\frac{1}{L} \sum_{\ell=1}^L \|\nabla_n \mathbf{u}_{\cdot, \ell}\|_2^2} + \epsilon^2 + \beta_{\text{sparse}} \sum_{n=1}^{N'} \sum_{\ell=1}^L |u_{n, \ell}|, \quad (26)$$

with $\nabla_n \mathbf{u}_{\cdot, \ell}$ the 2D spatial gradient at pixel n of the ℓ -th spectral channel, evaluated by finite differences, and ϵ a parameter chosen so as to be negligible compared to the average norm of the spatial gradient where there is a sharp edge (the regularization then approaches an isotropic vectorial total variation [34]) and similar to the gradient magnitude in smoothly-varying areas (this prevents the apparition of the staircasing effect common with total variation). Hyper-parameters β_{smooth} and β_{sparse} balance the weight of each regularization term with respect to the data-fitting term. Note that, due to the positivity constraint in equation (25), the L^1 norm $\|\mathbf{u}\|_1$ corresponds to the simple differentiable term $\sum_{n=1}^{N'} \sum_{\ell=1}^L u_{n, \ell}$ for any feasible object \mathbf{u} , and the regularization $\mathcal{R}(\mathbf{u})$ is differentiable.

C. Joint estimation of the statistics of nuisance terms and reconstruction of the component of interest

The estimation of the parameters of the statistical model for nuisance terms should be performed on data free of the component of interest, i.e., on the residuals $\mathbf{v} - \mathbf{M}\mathbf{u}$. Starting from an initial guess $\hat{\boldsymbol{\mu}}_n^{\text{spec}(0)}$, $\hat{\boldsymbol{\sigma}}_n^2(0)$, $\tilde{\mathbf{C}}_n^{\text{spec}(0)}$, and $\tilde{\mathbf{C}}_n^{\text{spat}(0)}$ computed under the assumption $\mathbf{u} = 0$ (i.e., directly on the data), reconstruction and estimation steps can be alternated to successively refine the contribution of the objects and the background statistics. In order to speed up the process, we consider a joint reconstruction and estimation approach. Since in section II-C we derived our estimators from the loss function \mathcal{D}_n (Proposition 4), we can perform jointly the

reconstruction and the estimation of the parameters of the nuisance model by minimizing a common cost function:

$$\hat{\mathbf{u}} = \arg \min_{\mathbf{u} \geq 0} \underbrace{\min_{\substack{\{\hat{\boldsymbol{\mu}}_n^{\text{spec}}\}_{n \in \mathbb{K}} \\ \{\hat{\boldsymbol{\sigma}}_n^2\}_{n \in \mathbb{K}} \\ \{\tilde{\mathbf{C}}_n^{\text{spec}}\}_{n \in \mathbb{K}} \\ \{\tilde{\mathbf{C}}_n^{\text{spat}}\}_{n \in \mathbb{K}}} \sum_{n \in \mathbb{K}} \mathcal{D}_n(\mathbf{v}_n - [\mathbf{M}\mathbf{u}]_n) + \mathcal{R}(\mathbf{u})}_{\mathcal{C}(\mathbf{u})}, \quad (27)$$

where the dependence of \mathcal{D}_n on parameters $\hat{\boldsymbol{\mu}}_n^{\text{spec}}$, $\hat{\boldsymbol{\sigma}}_n^2$, $\tilde{\mathbf{C}}_n^{\text{spec}}$, and $\tilde{\mathbf{C}}_n^{\text{spat}}$ is not explicitly written. In the expression of \mathcal{D}_n given in Proposition 4, the spatio-spectro-temporal patch \mathcal{D}_n is replaced by the residual patch $\mathbf{v}_n - [\mathbf{M}\mathbf{u}]_n$ obtained when removing the contribution of the component of interest.

To solve this hierarchical minimization problem, we suggest using a large-scale continuous optimization technique to solve the outer minimization problem and the fixed-point method based on Eqs.(19)–(22) to solve the inner problem. The following proposition gives the expression of the gradient of $\mathcal{C}(\mathbf{u})$.

Proposition 5 (Gradient of the cost function with respect to reconstructed component \mathbf{u}). *The gradient of the cost function $\mathcal{C}(\mathbf{u})$ with respect to \mathbf{u} is:*

$$\nabla_{\mathbf{u}} \mathcal{C}(\mathbf{u}) = \mathbf{M}^\top \sum_{n \in \mathbb{K}} \sum_{t=1}^T \frac{1}{\hat{\boldsymbol{\sigma}}_{n,t}^2(\mathbf{u})} \mathbf{P}_{n,t}^\top \hat{\mathbf{\Gamma}}_n(\mathbf{u}) [\mathbf{P}_{n,t} \mathbf{M} \mathbf{u} - (\mathbf{v}_{n,t} - \hat{\boldsymbol{\mu}}_n^{\text{spec}}(\mathbf{u}))] + \beta_{\text{smooth}} \sum_{n=1}^{N'} \frac{1}{2\sqrt{\sum_{\ell=1}^L \|\mathbf{D}_{n,\ell} \mathbf{u}\|_2^2 + \epsilon^2}} \mathbf{D}_{n,\ell}^\top \mathbf{D}_{n,\ell} \mathbf{u} + \beta_{\text{sparse}} \mathbf{1} \quad (28)$$

where $\mathbf{P}_{n,t}$ is the $KL \times KLT$ matrix that extracts a multi-spectral patch at spatial location n and time t , $\hat{\mathbf{\Gamma}}_n(\mathbf{u})$ is equal to $(\boldsymbol{\Psi}_n^{\text{spec}} \odot \tilde{\mathbf{C}}_n^{\text{spec}-1}(\mathbf{u})) \otimes (\boldsymbol{\Psi}_n^{\text{spat}} \odot \tilde{\mathbf{C}}_n^{\text{spat}-1}(\mathbf{u}))$, and $\mathbf{D}_{n,\ell}$ is the $2 \times N'L$ matrix that computes the horizontal and vertical finite differences at pixel n for the wavelength ℓ of the object.

Proof. The expression follows directly from differentiation rules by noting that the differentials with respect to parameters $\hat{\boldsymbol{\mu}}_n^{\text{spec}}(\mathbf{u})$, $\hat{\boldsymbol{\sigma}}_n^2(\mathbf{u})$, $\tilde{\mathbf{C}}_n^{\text{spec}}(\mathbf{u})$, $\tilde{\mathbf{C}}_n^{\text{spat}}(\mathbf{u})$ are all null due to Proposition 4. When applying the chain rule, the terms implying differentials of $\hat{\boldsymbol{\sigma}}_{n,t}^2(\mathbf{u})$, $\hat{\mathbf{\Gamma}}_n(\mathbf{u})$, or $\hat{\boldsymbol{\mu}}_n^{\text{spec}}(\mathbf{u})$ thus cancel out and only the terms where these parameters are considered fixed remain. \square

To solve the smooth optimization problem under bound constraints of Eq.(27), we use a limited-memory quasi-Newton method with bound constraints, VMLM-B [35], which is a more efficient variant of L-BFGS-B [36]. This algorithm evaluates the cost function $\mathcal{C}(\mathbf{u})$ and the gradient $\nabla_{\mathbf{u}} \mathcal{C}(\mathbf{u})$ given in Proposition 5 iteratively until reaching convergence to a local optimum.

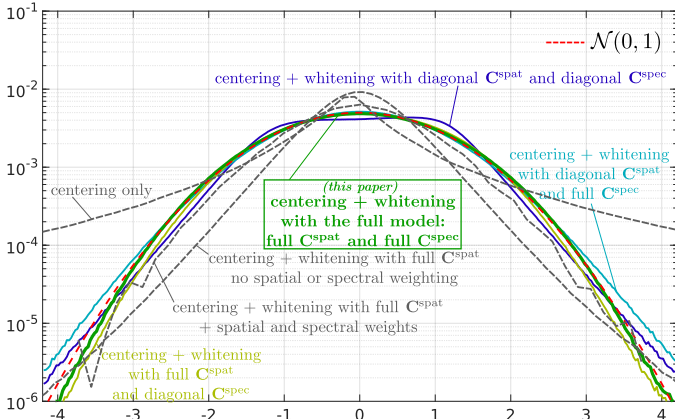


Fig. 3. Empirical distribution of the centered and whitened patches, for different covariance models.

IV. RESULTS

A. Validation of the statistical model of the nuisance component

Before evaluating the reconstruction method on high-contrast observations of circumstellar disks, we show that our statistical model of the nuisances is relevant. We consider the same ASDI dataset as in [25] (star HR 8799, with its three known exoplanets masked out so that the data correspond only to the nuisance term) and perform a similar analysis: we represent in Fig.3 the empirical distribution of the patches after performing different pre-processing. If random vectors \mathbf{v}_n are accurately modeled by a Gaussian distribution with mean $\boldsymbol{\mu}_n$ and covariance \mathbf{C}_n , as in equation (2), then the centered and whitened vectors $\mathbf{C}_n^{-1/2}(\mathbf{v}_n - \boldsymbol{\mu}_n)$ should follow $\mathcal{N}(\mathbf{0}, \mathbf{I})$. Therefore, we compare a standard Gaussian distribution with the empirical marginal distribution of $\mathbf{C}_n^{-1/2}(\mathbf{v}_n - \boldsymbol{\mu}_n)$ for several covariance models: the three models considered in [25], drawn in gray dashed-lines: (i) no covariance ($\mathbf{C}_n = \mathbf{I}$); (ii) only spatial covariances; (iii) spatial covariances + temporal and spectral weighting; and four additional models: (iv) diagonal spatial and spectral covariances (i.e., spatial, spectral, and temporal weighting via a separable model); (v) full spatial covariance, diagonal spectral covariance, and temporal weighting; (vi) full spectral covariance, diagonal spatial covariance, and temporal weighting; and finally (vii) the full separable model introduced in this paper (see equation (4)). The centered and whitened patches are best modeled with the full model (the green curve is the closest to the red dashed-line corresponding to the standard Gaussian distribution), which justifies its use in our loss function \mathcal{D}_n . We give a more detailed study of the empirical distribution of patches in the Supplementary Material associated with this paper.

The shrinkage parameters ρ_n^{spat} and ρ_n^{spec} may have a significant impact on the statistical model. We monitor their values by displaying maps of the spatial and spectral shrinkage parameters in Fig.4 for the dataset shown in Fig.1. Values of ρ_n^{spat} and ρ_n^{spec} remain small (below 0.13), which indicates a moderate bias toward 0. The spatial shrinkage is stronger at the borders of the field-of-view where there are fewer samples available due to the spectral scaling. Spectral shrinkage is

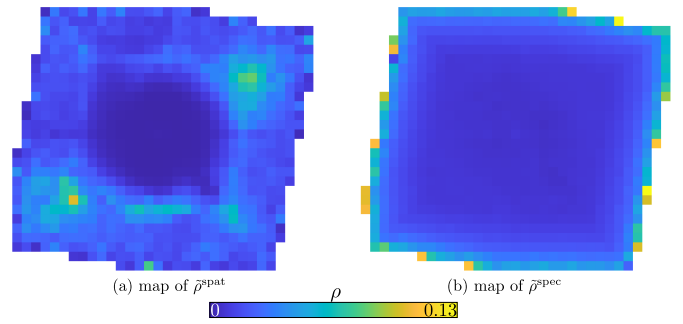


Fig. 4. Spatial distribution of the spatial and spectral shrinkage parameters.

stronger for this dataset at some locations of the field-of-view which shows that setting a global shrinkage value for the whole field-of-view would be sub-optimal.

B. Reconstruction of disks from VLT/SPHERE-IFS data

Now, we consider two datasets resulting from the observation of two different stars hosting a known circumstellar disk: SAO 206462 (already shown in Fig.1, observation date: 2015-05-15, ESO program: 095.C-0298) which contains a spiral disk and HR 4796 (observation date: 2015-02-02, ESO program: 095.C-0298) with a thin elliptical disk.

We first perform an ablation study by showing how the reconstruction results are impacted if simpler covariance models are considered rather than the full model of equation (4). Fig.5 displays the reconstructed disk component in four cases, from left to right: (i) no modeling of spatial or spectral correlations; (ii) modeling only of spatial correlations; (iii) modeling only of spectral correlations; and (iv) the full model proposed in this paper. The dataset HR 4796 suffers from a strong nuisance component. Failing to account for the spatial correlations leads to severe artifacts: a ghost circular structure is reconstructed. By closely inspecting the center of the field-of-view of SAO 206462, the presence of spurious structures can be noted in all reconstructions except the reconstruction with the full model. These qualitative assessments indicate that the modeling of correlations is beneficial to the reconstructions.

Fig.6 shows reconstructions obtained by several reference methods along with reconstructions obtained with our method. Since other methods do not perform a deconvolution, we show in the fourth column of Fig.6 our reconstruction re-blurred at the resolution of the instrument (i.e., $\mathbf{B}\hat{\mathbf{u}}$ rather than $\hat{\mathbf{u}}$). Three methods were considered as reference: cADI [2] which estimates the nuisance component by temporally stacking the observations (using medians), PCA ADI [7] which uses a principal component analysis to remove the nuisance component (the best number of modes has been manually selected by trial and error), and PACO ASDI [25] which was originally designed to extract exoplanets from ASDI datasets but can also partially reconstruct thin disks. For cADI and PCA ADI, we use the official implementations of the SPHERE data center [37], [38], while we use our unsupervised pipeline of PACO ASDI [25]. The reconstructions obtained with the reference methods all suffer from artifacts, in particular in the center of the field-of-view. In comparison, the blurred and the

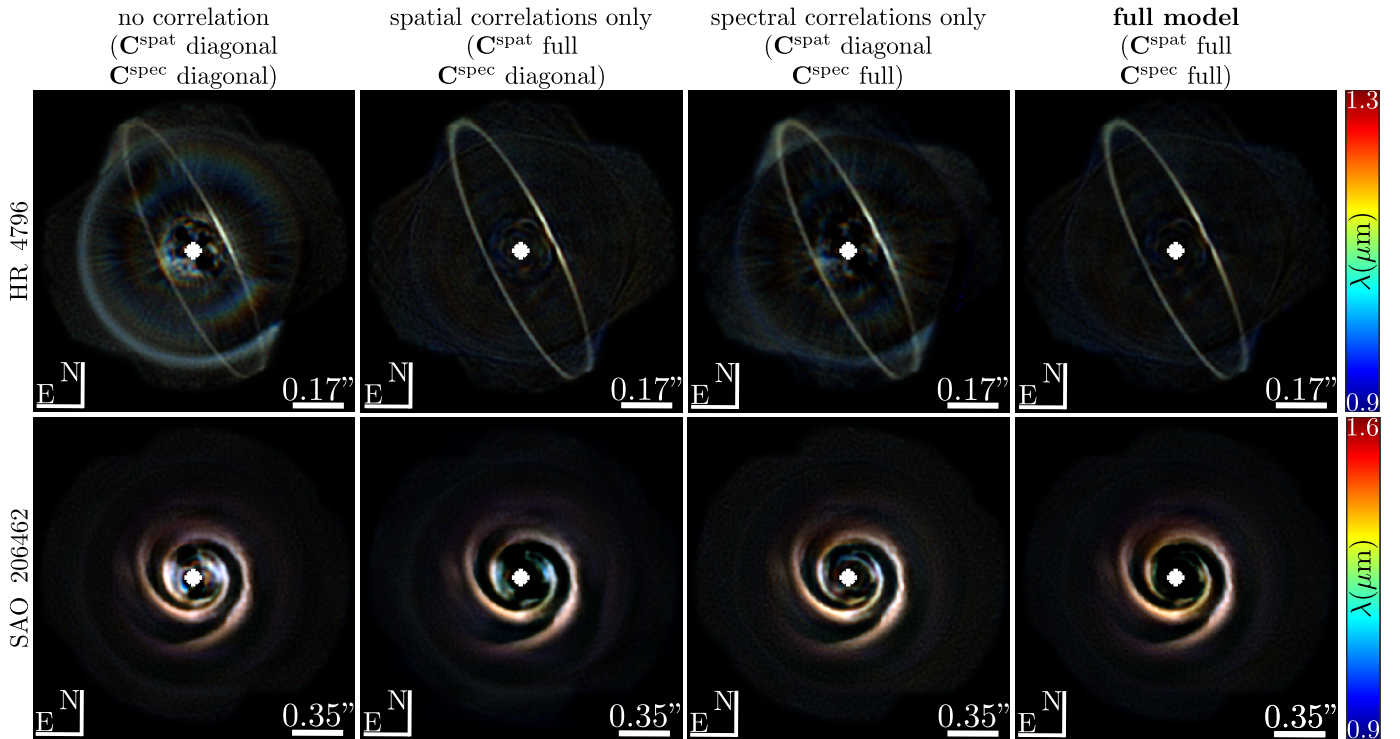


Fig. 5. Ablation study: neglecting the spatial and/or spectral correlations of the nuisance component negatively affects the reconstruction results. The images shown correspond to the deconvolved reconstructions \hat{u} . Fake RGB images are shown with colors selected to cover the infrared spectrum according to the colormaps on the right.

deblurred reconstructions shown in the last two columns of Fig. 6 are much more satisfactory: the structure of the disks is in good match with standard models of circumstellar disks [39], [40]. Besides, the REXPACO ASDI reconstruction of HR 4796 (respectively, SAO 206462) can be compared qualitatively with the reconstruction given in Fig.4 (respectively, Fig.1 bottom-left) of [39] (respectively, of [40]) obtained using customized routines of cADI on the same datasets considered in this paper. The REXPACO ASDI reconstructions exhibits significantly less artifacts such as non-physical discontinuities in the disk structures and residuals stellar leakages near the star. The deconvolution step of the proposed method also leads to an improved resolution of the thin structures of the disks. Reference methods cADI and PCA ADI subtract part of the disk component when removing the nuisance term. This leads to strong flux biases and a high-pass filtering effect. PACO ASDI is designed to detect point-like structures, it recovers parts of the disks in large gradient areas: it is much more successful on the thin disk of HR 4796 than on the thicker spiral disk of SAO 206462. Finally, the multi-spectral REXPACO ASDI reconstructions of Fig.6 can be compared with the mono-spectral reconstructions obtained with the REXPACO algorithm [14] (see Fig.11 of [14]) on mono-spectral datasets of the same target stars. These mono-spectral datasets were recorded by the InfraRed Dual Imaging Spectrograph (IRDIS) of the SPHERE instrument operating simultaneously with the IFS but in a different spectral band and resolution. A joint processing of multi-spectral datasets is particularly relevant for disks having a circular symmetry, like SAO 206462, since it helps to unmix the light coming from the disk and the

star light (since the two components not always superimposed due to the chromatic scaling of speckles). This joint multi-processing leads to a better rejection of the noise thus limiting the non-physical reconstruction artifacts like discontinuities in the spiral arms.

V. CONCLUSION

Correlations of the noise (or of a nuisance component) are generally neglected when solving an image reconstruction problem. If not, a stationarity assumption is typically used to model and compensate for these correlations. In this paper, we considered an application in which the nuisance component has a strong non-stationarity. We resorted to a local modeling of the spatial and spectral correlations to achieve a more accurate statistical description of the data and obtain reconstructions without noticeable artifacts. Our modeling of these correlations is based on a separable approximation to reduce the number of free parameters. We developed estimators based on shrinkage covariance estimators and a compound-Gaussian model to reduce estimation variance and improve robustness. These mean and covariance estimators of our statistical model of nuisances are evaluated jointly to the reconstruction of the component of interest. This leads to an algorithm that scales to the size of typical ASDI datasets.

We have shown on several datasets obtained with the SPHERE-IFS instrument at the VLT, in Chile, that much improved reconstructions of circumstellar disks could be obtained with our method. This will help astrophysicists better understand the phenomena that govern the formation of planetary systems and the interactions between exoplanets and dust

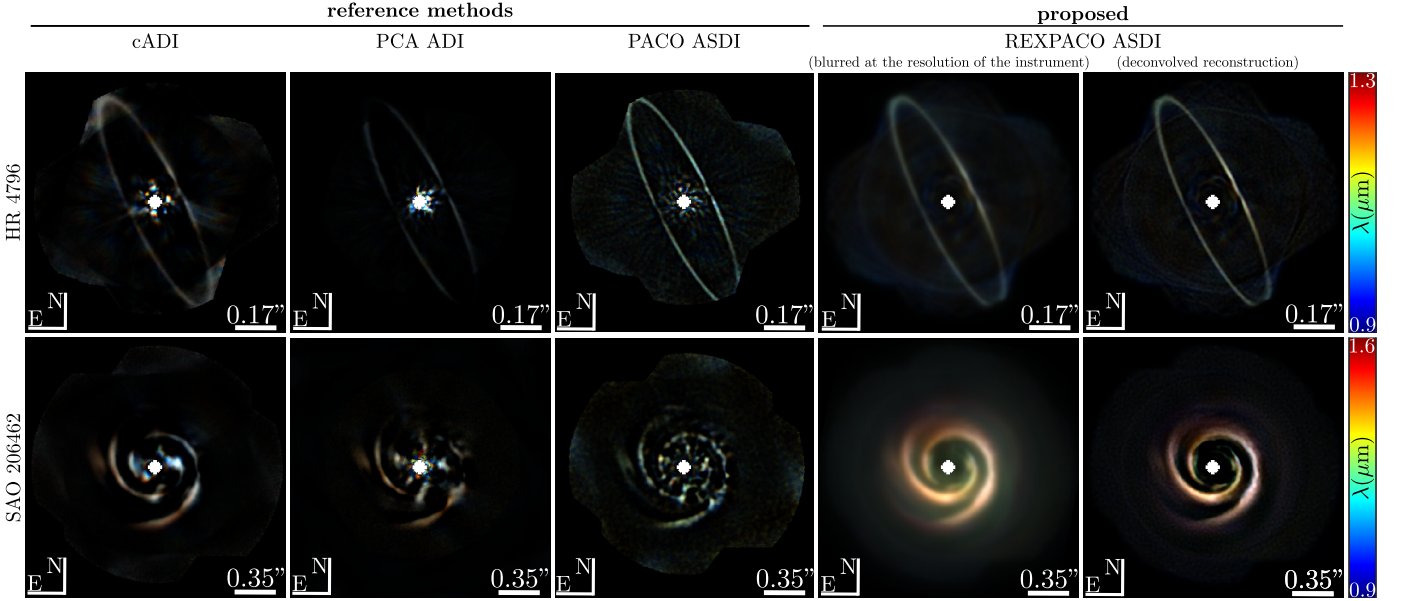


Fig. 6. Disk reconstruction results. The images shown for the method REXPACO ASDI in the fourth column are re-blurred to be easier to compare with the reference methods (i.e., they correspond to $\mathbf{B}\hat{\mathbf{u}}$). Deblurred results $\hat{\mathbf{u}}$ are shown on the last column (they correspond to the last column of Fig.5). Fake colors are used as in the previous figure.

disks. Beyond its use in astronomy, we think that this general approach of modeling spatial and spectral correlations in an image reconstruction problem could also be applied to other fields of imaging such as microscopy.

APPENDIX A

PROOF OF THE MLES GIVEN IN PROPOSITION 1

Under the assumptions of section II-B, the co-log-likelihood of the 4D patch \mathbf{v}_n , in the absence of disk or exoplanet, writes:

$$\begin{aligned} \mathcal{L} &= -\log p_{V_n}(\mathbf{v}_n) \\ &= \frac{TK}{2} \log |\mathbf{C}_n^{\text{spec}}| + \frac{TL}{2} \log |\mathbf{C}_n^{\text{spat}}| + \sum_{t=1}^T \left(\frac{KL}{2} \log \sigma_{n,t}^2 + \right. \\ &\quad \left. + \frac{1}{2\sigma_{n,t}^2} \|\mathbf{v}_{n,t} - \boldsymbol{\mu}_n^{\text{spec}}\|_{(\mathbf{C}_n^{\text{spec}} \otimes \mathbf{C}_n^{\text{spat}})^{-1}}^2 \right), \end{aligned} \quad (29)$$

where we used the following properties of the Kronecker product: $|\mathbf{A} \otimes \mathbf{B}| = |\mathbf{A}|^m |\mathbf{B}|^n$ (with \mathbf{A} an $n \times n$ matrix and \mathbf{B} an $m \times m$ matrix) and $(\mathbf{A} \otimes \mathbf{B})^{-1} = \mathbf{A}^{-1} \otimes \mathbf{B}^{-1}$.

To obtain the MLEs, we differentiate \mathcal{L} :

$$\begin{aligned} \partial \mathcal{L} &= \frac{TK}{2} \text{tr}(\mathbf{C}_n^{\text{spec}}^{-1} \partial \mathbf{C}_n^{\text{spec}}) + \frac{TL}{2} \text{tr}(\mathbf{C}_n^{\text{spat}}^{-1} \partial \mathbf{C}_n^{\text{spat}}) \\ &+ \sum_{t=1}^T \left\{ \frac{KL}{2} \frac{\partial \sigma_{n,t}^2}{\sigma_{n,t}^2} - \frac{\partial \sigma_{n,t}^2}{2\sigma_{n,t}^4} \|\mathbf{v}_{n,t} - \boldsymbol{\mu}_n^{\text{spec}}\|_{\mathbf{C}_n^{\text{spec}}^{-1} \otimes \mathbf{C}_n^{\text{spat}}^{-1}}^2 \right. \\ &\quad + \frac{1}{\sigma_{n,t}^2} (\boldsymbol{\mu}_n^{\text{spec}} - \mathbf{v}_{n,t})^\top (\mathbf{C}_n^{\text{spec}}^{-1} \otimes \mathbf{C}_n^{\text{spat}}^{-1}) \partial \boldsymbol{\mu}_n^{\text{spec}} \\ &\quad - \frac{1}{2\sigma_{n,t}^2} \text{tr} \left(\mathbf{C}_n^{\text{spec}}^{-1} \partial \mathbf{C}_n^{\text{spec}} \mathbf{C}_n^{\text{spec}}^{-1} \bar{\mathbf{V}}_t^\top \mathbf{C}_n^{\text{spat}}^{-1} \bar{\mathbf{V}}_t \right) \\ &\quad \left. - \frac{1}{2\sigma_{n,t}^2} \text{tr} \left(\mathbf{C}_n^{\text{spat}}^{-1} \partial \mathbf{C}_n^{\text{spat}} \mathbf{C}_n^{\text{spat}}^{-1} \bar{\mathbf{V}}_t \mathbf{C}_n^{\text{spec}}^{-1} \bar{\mathbf{V}}_t^\top \right) \right\} \end{aligned} \quad (30)$$

where we obtained the last two terms by rewriting the squared norm $\|\mathbf{v}_{n,t} - \boldsymbol{\mu}_n^{\text{spec}}\|_{\mathbf{C}_n^{\text{spec}}^{-1} \otimes \mathbf{C}_n^{\text{spat}}^{-1}}^2$ under the form

$\text{tr}(\bar{\mathbf{V}}_t^\top \mathbf{C}_n^{\text{spat}}^{-1} \bar{\mathbf{V}}_t \mathbf{C}_n^{\text{spec}}^{-1})$, with $\bar{\mathbf{V}}_t$ the $K \times L$ matrix whose element at row k and column ℓ is $[\mathbf{v}_{n,t}]_{k,\ell} - [\boldsymbol{\mu}_n^{\text{spec}}]_{k,\ell}$.

The following set of conditions is sufficient for $\partial \mathcal{L}$ to be equal to zero:

$$\sum_{t=1}^T \frac{1}{\sigma_{n,t}^2} (\boldsymbol{\mu}_n^{\text{spec}} - \mathbf{v}_{n,t}) = 0 \quad (31a)$$

$$\frac{KL}{2} \frac{1}{\sigma_{n,t}^2} - \frac{1}{2\sigma_{n,t}^4} \|\mathbf{v}_{n,t} - \boldsymbol{\mu}_n^{\text{spec}}\|_{\mathbf{C}_n^{\text{spec}}^{-1} \otimes \mathbf{C}_n^{\text{spat}}^{-1}}^2 = 0 \quad (31b)$$

$$\frac{TK}{2} \mathbf{I} - \sum_{t=1}^T \frac{1}{2\sigma_{n,t}^2} \mathbf{C}_n^{\text{spec}}^{-1} \bar{\mathbf{V}}_t^\top \mathbf{C}_n^{\text{spat}}^{-1} \bar{\mathbf{V}}_t = \mathbf{0} \quad (31c)$$

$$\frac{TL}{2} \mathbf{I} - \sum_{t=1}^T \frac{1}{2\sigma_{n,t}^2} \mathbf{C}_n^{\text{spat}}^{-1} \bar{\mathbf{V}}_t \mathbf{C}_n^{\text{spec}}^{-1} \bar{\mathbf{V}}_t^\top = \mathbf{0} \quad (31d)$$

Condition (31a) holds if:

$$\hat{\boldsymbol{\mu}}_n^{\text{spec}} = \left(\sum_{t=1}^T \sigma_{n,t}^{-2} \mathbf{v}_{n,t} \right) / \left(\sum_{t=1}^T \sigma_{n,t}^{-2} \right). \quad (32)$$

Condition (31b) holds if:

$$\hat{\sigma}_{n,t}^2 = \frac{1}{KL} \|\mathbf{v}_{n,t} - \hat{\boldsymbol{\mu}}_n^{\text{spec}}\|_{\mathbf{C}_n^{\text{spec}}^{-1} \otimes \hat{\mathbf{C}}_n^{\text{spat}}^{-1}}^2. \quad (33)$$

Condition (31c) holds if:

$$\hat{\mathbf{C}}_n^{\text{spec}} = \frac{1}{TK} \sum_{t=1}^T \frac{1}{\hat{\sigma}_{n,t}^2} \bar{\mathbf{V}}_t^\top \hat{\mathbf{C}}_n^{\text{spat}}^{-1} \bar{\mathbf{V}}_t. \quad (34)$$

Condition (31d) holds if:

$$\hat{\mathbf{C}}_n^{\text{spat}} = \frac{1}{TL} \sum_{t=1}^T \frac{1}{\hat{\sigma}_{n,t}^2} \bar{\mathbf{V}}_t \hat{\mathbf{C}}_n^{\text{spec}}^{-1} \bar{\mathbf{V}}_t^\top. \quad (35)$$

These correspond to the expressions given in Proposition 1.

APPENDIX B
PROOF OF PROPOSITION 3

We start by rewriting the L^2 norm under the form of a trace:

$$\sum_{t=1}^T \frac{1}{2\sigma_{n,t}^2} \|\mathbf{v}_{n,t} - \boldsymbol{\mu}_n\|_{\Gamma}^2 = \text{tr} \left((\boldsymbol{\Psi}_n \odot (\mathbf{C}^{-1})) \sum_{t=1}^T \frac{1}{2\sigma_{n,t}^2} (\mathbf{v}_{n,t} - \boldsymbol{\mu}_n)(\mathbf{v}_{n,t} - \boldsymbol{\mu}_n)^{\top} \right) \quad (36)$$

$$= \text{tr} \left[\mathbf{C}^{-1} \left(\boldsymbol{\Psi}_n \odot \sum_{t=1}^T \frac{1}{2\sigma_{n,t}^2} (\mathbf{v}_{n,t} - \boldsymbol{\mu}_n)(\mathbf{v}_{n,t} - \boldsymbol{\mu}_n)^{\top} \right) \right]. \quad (37)$$

The differential of the cost function introduced in Proposition 3, when all other parameters are fixed, writes:

$$\partial \left[\frac{T}{2} \log |\mathbf{C}| + \sum_{t=1}^T \frac{1}{2\sigma_{n,t}^2} \|\mathbf{v}_{n,t} - \boldsymbol{\mu}_n\|_{\Gamma}^2 \right] = \frac{T}{2} \text{tr}(\mathbf{C}^{-1} \partial \mathbf{C}) + \text{tr} \left[\mathbf{C}^{-1} \partial \mathbf{C} \mathbf{C}^{-1} \left(\boldsymbol{\Psi}_n \odot \sum_{t=1}^T \frac{1}{2\sigma_{n,t}^2} (\mathbf{v}_{n,t} - \boldsymbol{\mu}_n)(\mathbf{v}_{n,t} - \boldsymbol{\mu}_n)^{\top} \right) \right] \quad (38)$$

A sufficient condition for the differential to be equal to zero is:

$$\frac{T}{2} \mathbf{I} + \mathbf{C}^{-1} \left(\boldsymbol{\Psi}_n \odot \sum_{t=1}^T \frac{1}{2\sigma_{n,t}^2} (\mathbf{v}_{n,t} - \boldsymbol{\mu}_n)(\mathbf{v}_{n,t} - \boldsymbol{\mu}_n)^{\top} \right) = \mathbf{0} \quad (39)$$

which holds if:

$$\mathbf{C} = \boldsymbol{\Psi}_n \odot \frac{1}{T} \sum_{t=1}^T \frac{1}{\sigma_{n,t}^2} (\mathbf{v}_{n,t} - \boldsymbol{\mu}_n)(\mathbf{v}_{n,t} - \boldsymbol{\mu}_n)^{\top}. \quad (40)$$

This is equivalent to the definition of the shrinkage covariance matrix estimator of Proposition 2 since the weighting matrix $\boldsymbol{\Psi}_n$ is defined as the $D \times D$ matrix with 1 on the diagonal and the value $(1 - \hat{\rho}_n)$ off the diagonal, and $\hat{\rho}_n$ is computed according to Eq.(12).

APPENDIX C
PROOF OF PROPOSITION 4

As stated in Proposition 4, we consider the shrinkage matrices $\boldsymbol{\Psi}^{\text{spec}}$ and $\boldsymbol{\Psi}^{\text{spat}}$ to be fixed (i.e., $\hat{\rho}_n^{\text{spec}}$ and $\hat{\rho}_n^{\text{spat}}$ are estimated once for all).

Before computing the differential of \mathcal{D}_n , note that its last term, $\frac{1}{2\sigma_{n,t}^2} \|\mathbf{v}_{n,t} - \boldsymbol{\mu}_n^{\text{spec}}\|_{\Gamma}^2$, can be rewritten in several different ways using the following identities:

$$\|\mathbf{a}\|_{(\boldsymbol{\Psi}_1 \otimes \boldsymbol{\Psi}_2) \odot (\Gamma_1 \otimes \Gamma_2)}^2 = \|\mathbf{a}\|_{(\boldsymbol{\Psi}_1 \odot \Gamma_1) \otimes (\boldsymbol{\Psi}_2 \odot \Gamma_2)}^2 = \text{tr}[\mathbf{a} \mathbf{a}^{\top}] \quad (41)$$

$$= \text{tr}[\mathbf{a} \mathbf{a}^{\top}] \quad (42)$$

$$= \text{tr}[(\boldsymbol{\Psi}_1 \otimes \boldsymbol{\Psi}_2) \odot (\Gamma_1 \otimes \Gamma_2)] \mathbf{a} \mathbf{a}^{\top} \quad (43)$$

$$= \text{tr}[(\boldsymbol{\Psi}_1 \otimes \boldsymbol{\Psi}_2) \odot (\mathbf{A} \mathbf{A}^{\top})] \quad (44)$$

$$= \text{tr}[\mathbf{A}^{\top} (\boldsymbol{\Psi}_2 \odot \Gamma_2) \mathbf{A} (\boldsymbol{\Psi}_1 \odot \Gamma_1)] \quad (45)$$

$$= \text{tr}[\Gamma_2 (\boldsymbol{\Psi}_2 \odot (\mathbf{A} (\boldsymbol{\Psi}_1 \odot \Gamma_1) \mathbf{A}^{\top}))] \quad (46)$$

$$= \text{tr}[\Gamma_1 (\boldsymbol{\Psi}_1 \odot (\mathbf{A}^{\top} (\boldsymbol{\Psi}_2 \odot \Gamma_2) \mathbf{A}))], \quad (46)$$

where \mathbf{A} is a $m \times n$ matrix obtained by reshaping the column vector \mathbf{a} according to the dimensions of matrices $\Gamma_1 \in \mathbb{R}^{n \times n}$ and $\Gamma_2 \in \mathbb{R}^{m \times m}$, such that $\text{vec}(\mathbf{A}) = \mathbf{a}$.

The total differential of the cost function \mathcal{D}_n , for fixed matrices $\boldsymbol{\Psi}^{\text{spec}}$ and $\boldsymbol{\Psi}^{\text{spat}}$, is:

$$\begin{aligned} \partial \mathcal{D}_n &= \frac{TK}{2} \text{tr}(\mathbf{C}_n^{\text{spec}-1} \partial \mathbf{C}_n^{\text{spec}}) + \frac{TL}{2} \text{tr}(\mathbf{C}_n^{\text{spat}-1} \partial \mathbf{C}_n^{\text{spat}}) \\ &+ \sum_{t=1}^T \left(\frac{KL}{2} \frac{\partial \sigma_{n,t}^2}{\sigma_{n,t}^2} - \frac{\partial \sigma_{n,t}^2}{2\sigma_{n,t}^4} \|\mathbf{v}_{n,t} - \boldsymbol{\mu}_n^{\text{spec}}\|_{\Gamma}^2 \right. \\ &\quad \left. + \frac{1}{\sigma_{n,t}^2} (\boldsymbol{\mu}_n^{\text{spec}} - \mathbf{v}_{n,t})^{\top} \Gamma \partial \boldsymbol{\mu}_n^{\text{spec}} \right. \\ &- \frac{1}{2\sigma_{n,t}^2} \text{tr} \left[\mathbf{C}_n^{\text{spec}-1} \partial \mathbf{C}_n^{\text{spec}} \mathbf{C}_n^{\text{spec}-1} \left\{ \boldsymbol{\Psi}_n^{\text{spec}} \odot (\bar{\mathbf{V}}_t^{\top} (\boldsymbol{\Psi}_n^{\text{spat}} \odot \mathbf{C}_n^{\text{spat}-1}) \bar{\mathbf{V}}_t) \right\} \right] \\ &- \frac{1}{2\sigma_{n,t}^2} \text{tr} \left[\mathbf{C}_n^{\text{spat}-1} \partial \mathbf{C}_n^{\text{spat}} \mathbf{C}_n^{\text{spat}-1} \left\{ \boldsymbol{\Psi}_n^{\text{spat}} \odot (\bar{\mathbf{V}}_t (\boldsymbol{\Psi}_n^{\text{spec}} \odot \mathbf{C}_n^{\text{spec}-1}) \bar{\mathbf{V}}_t^{\top}) \right\} \right] \Big], \quad (47) \end{aligned}$$

where $\bar{\mathbf{V}}_t$ represents the spatio-spectral patch in matrix form (see Proposition 1).

The following set of conditions is sufficient for $\partial \mathcal{D}_n$ to be equal to zero:

$$\sum_{t=1}^T \frac{1}{\sigma_{n,t}^2} (\boldsymbol{\mu}_n^{\text{spec}} - \mathbf{v}_{n,t}) = \mathbf{0} \quad (48a)$$

$$KL\sigma_{n,t}^2 - \|\mathbf{v}_{n,t} - \boldsymbol{\mu}_n^{\text{spec}}\|_{\Gamma}^2 = 0 \quad (48b)$$

$$\frac{TK}{2} \mathbf{I} - \sum_{t=1}^T \frac{1}{2\sigma_{n,t}^2} \mathbf{C}_n^{\text{spec}-1} \left\{ \boldsymbol{\Psi}_n^{\text{spec}} \odot (\bar{\mathbf{V}}_t^{\top} (\boldsymbol{\Psi}_n^{\text{spat}} \odot \mathbf{C}_n^{\text{spat}-1}) \bar{\mathbf{V}}_t) \right\} = \mathbf{0} \quad (48c)$$

$$\frac{TL}{2} \mathbf{I} - \sum_{t=1}^T \frac{1}{2\sigma_{n,t}^2} \mathbf{C}_n^{\text{spat}-1} \left\{ \boldsymbol{\Psi}_n^{\text{spat}} \odot (\bar{\mathbf{V}}_t (\boldsymbol{\Psi}_n^{\text{spec}} \odot \mathbf{C}_n^{\text{spec}-1}) \bar{\mathbf{V}}_t^{\top}) \right\} = \mathbf{0} \quad (48d)$$

Condition (48a) holds if:

$$\hat{\boldsymbol{\mu}}_n^{\text{spec}} = \left(\sum_{t=1}^T \frac{1}{\sigma_{n,t}^2} \mathbf{v}_{n,t} \right) / \left(\sum_{t=1}^T \frac{1}{\sigma_{n,t}^2} \right). \quad (49)$$

Condition (48b) holds if:

$$\hat{\sigma}_{n,t}^2 = \frac{1}{KL} \|\mathbf{v}_{n,t} - \boldsymbol{\mu}_n^{\text{spec}}\|_{\Gamma}^2. \quad (50)$$

Condition (48c) holds if:

$$\hat{\mathbf{C}}_n^{\text{spec}} = \frac{1}{TK} \sum_{t=1}^T \frac{1}{\hat{\sigma}_{n,t}^2} \boldsymbol{\Psi}_n^{\text{spec}} \odot (\bar{\mathbf{V}}_t^{\top} (\boldsymbol{\Psi}_n^{\text{spat}} \odot \mathbf{C}_n^{\text{spat}-1}) \bar{\mathbf{V}}_t). \quad (51)$$

Condition (48d) holds if:

$$\hat{\mathbf{C}}_n^{\text{spat}} = \frac{1}{TL} \sum_{t=1}^T \frac{1}{\hat{\sigma}_{n,t}^2} \boldsymbol{\Psi}_n^{\text{spat}} \odot (\bar{\mathbf{V}}_t (\boldsymbol{\Psi}_n^{\text{spec}} \odot \mathbf{C}_n^{\text{spec}-1}) \bar{\mathbf{V}}_t^{\top}). \quad (52)$$

These correspond to the expressions given in Proposition 4.

ACKNOWLEDGMENT

This work has been supported by the Région Auvergne-Rhône-Alpes under the project DIAGHOLO. This work has made use of the SPHERE Data Center, jointly operated by OSUG/IPAG (Grenoble, France), PYTHEAS/LAM/CESAM (Marseille, France), OCA/Lagrange (Nice, France), Observatoire de Paris/LESIA (Paris, France), and Observatoire de Lyon/CRAL (Lyon, France).

REFERENCES

- [1] M. Perryman, *The exoplanet handbook*. Cambridge University Press, 2018.
- [2] C. Marois, D. Lafrenière, R. Doyon, B. Macintosh, and D. Nadeau, “Angular differential imaging: A powerful high-contrast imaging technique,” *The Astrophysical Journal*, vol. 641, no. 1, p. 556, 2006.
- [3] R. Racine, G. A. Walker, D. Nadeau, R. Doyon, and C. Marois, “Speckle noise and the detection of faint companions,” *Publications of the Astronomical Society of the Pacific*, vol. 111, no. 759, p. 587, 1999.
- [4] D. Lafrenière, C. Marois, R. Doyon, D. Nadeau, and E. Artigau, “A new algorithm for point-spread function subtraction in high-contrast imaging: a demonstration with angular differential imaging,” *The Astrophysical Journal*, vol. 660, no. 1, p. 770, 2007.
- [5] C. Marois, C. Correia, J.-P. Véran, and T. Currie, “TLOCI: A fully loaded speckle killing machine,” *International Astronomical Union*, vol. 8, no. S299, pp. 48–49, 2013.
- [6] C. Marois, C. Correia, R. Galicher, P. Ingraham, B. Macintosh, T. Currie, and R. De Rosa, “GPI PSF subtraction with TLOCI: the next evolution in exoplanet/disk high-contrast imaging,” in *SPIE Astronomical Instrumentation + Telescopes*, vol. 9148. International Society for Optics and Photonics, 2014, p. 91480U.
- [7] R. Soummer, L. Pueyo, and J. Larkin, “Detection and characterization of exoplanets and disks using projections on Karhunen-Loève eigenimages,” *The Astrophysical Journal Letters*, vol. 755, no. 2, p. L28, 2012.
- [8] A. Amara and S. P. Quanz, “PYNPOINT: an image processing package for finding exoplanets,” *Monthly Notices of the Royal Astronomical Society*, vol. 427, no. 2, pp. 948–955, 2012.
- [9] J. Milli, D. Mouillet, A.-M. Lagrange, A. Boccaletti, D. Mawet, G. Chauvin, and M. Bonnefoy, “Impact of angular differential imaging on circumstellar disk images,” *Astronomy & Astrophysics*, vol. 545, p. A111, 2012.
- [10] B. Pairet, L. Jacques, and F. Cantalloube, “Iterative low-rank and rotating sparsity promotion for circumstellar disks imaging,” in *Signal Processing with Adaptive Sparse Structured Representations*, vol. 1, 2019, p. 1.
- [11] T. M. Esposito, M. P. Fitzgerald, J. R. Graham, and P. Kalas, “Modeling self-subtraction in angular differential imaging: Application to the HD 32297 debris disk,” *The Astrophysical Journal*, vol. 780, no. 1, p. 25, 2013.
- [12] Z. Wahhaj, J. Milli, C. Romero, L. Cieza, A. Zurlo, A. Vigan, E. Peña, G. Valdes, F. Cantalloube, J. Girard *et al.*, “A search for a fifth planet around HR 8799 using the star-hopping RDI technique at VLT/SPHERE,” *Astronomy & Astrophysics*, vol. 648, p. A26, 2021.
- [13] B. Pairet, F. Cantalloube, and L. Jacques, “MAYONNAISE: a morphological components analysis pipeline for circumstellar discs and exoplanets imaging in the near-infrared,” *Monthly Notices of the Royal Astronomical Society*, vol. 503, no. 3, pp. 3724–3742, 2021.
- [14] O. Flasseur, S. Thé, L. Denis, É. Thiébaud, and M. Langlois, “REX-PACO: An algorithm for high contrast reconstruction of the circumstellar environment by angular differential imaging,” *Astronomy & Astrophysics*, vol. 651, p. A62, 2021.
- [15] O. Flasseur, L. Denis, É. Thiébaud, and M. Langlois, “Exoplanet detection in angular differential imaging by statistical learning of the nonstationary patch covariances - The PACO algorithm,” *Astronomy & Astrophysics*, vol. 618, p. A138, 2018.
- [16] J.-L. Beuzit, A. Vigan, D. Mouillet, K. Dohlen, R. Gratton, A. Boccaletti, J.-F. Sauvage, H. M. Schmid, M. Langlois, C. Petit *et al.*, “SPHERE: the exoplanet imager for the Very Large Telescope,” *Astronomy & Astrophysics*, vol. 631, p. A155, 2019.
- [17] A. Buades, B. Coll, and J.-M. Morel, “A non-local algorithm for image denoising,” in *IEEE Computer Society Conference on Computer Vision and Pattern Recognition*, vol. 2. IEEE, 2005, pp. 60–65.
- [18] K. Dabov, A. Foi, V. Katkovnik, and K. Egiazarian, “Image denoising by sparse 3-D transform-domain collaborative filtering,” *IEEE Transactions on Image Processing*, vol. 16, no. 8, pp. 2080–2095, 2007.
- [19] M. Aharon, M. Elad, and A. Bruckstein, “K-SVD: An algorithm for designing overcomplete dictionaries for sparse representation,” *IEEE Transactions on Signal Processing*, vol. 54, no. 11, pp. 4311–4322, 2006.
- [20] J. Mairal, F. Bach, J. Ponce, G. Sapiro, and A. Zisserman, “Non-local sparse models for image restoration,” in *IEEE International Conference on Computer Vision*. IEEE, 2009, pp. 2272–2279.
- [21] D. Zoran and Y. Weiss, “From learning models of natural image patches to whole image restoration,” in *IEEE International Conference on Computer Vision*. IEEE, 2011, pp. 479–486.
- [22] G. Yu, G. Sapiro, and S. Mallat, “Solving inverse problems with piecewise linear estimators: From Gaussian mixture models to structured sparsity,” *IEEE Transactions on Image Processing*, vol. 21, no. 5, pp. 2481–2499, 2011.
- [23] M. Lebrun, A. Buades, and J.-M. Morel, “A nonlocal Bayesian image denoising algorithm,” *SIAM Journal on Imaging Sciences*, vol. 6, no. 3, pp. 1665–1688, 2013.
- [24] O. Flasseur, L. Denis, É. Thiébaud, and M. Langlois, “An unsupervised patch-based approach for exoplanet detection by direct imaging,” in *IEEE International Conference on Image Processing*. IEEE, 2018, pp. 2735–2739.
- [25] —, “PACO ASDI: an algorithm for exoplanet detection and characterization in direct imaging with integral field spectrographs,” *Astronomy & Astrophysics*, vol. 637, p. A9, 2020.
- [26] E. Conte, M. Lops, and G. Ricci, “Asymptotically optimum radar detection in compound-Gaussian clutter,” *IEEE Transactions on Aerospace and Electronic Systems*, vol. 31, no. 2, pp. 617–625, 1995.
- [27] M. J. Wainwright and E. P. Simoncelli, “Scale mixtures of Gaussians and the statistics of natural images,” in *Neural Information Processing Systems*, vol. 12, 1999, pp. 855–861.
- [28] O. Flasseur, L. Denis, É. Thiébaud, and M. Langlois, “Robustness to bad frames in angular differential imaging: a local weighting approach,” *Astronomy & Astrophysics*, vol. 634, p. A2, 2020.
- [29] N. Lu and D. L. Zimmerman, “The likelihood ratio test for a separable covariance matrix,” *Statistics & Probability Letters*, vol. 73, no. 4, pp. 449–457, 2005.
- [30] M. G. Genton, “Separable approximations of space-time covariance matrices,” *Environmetrics: The official Journal of the International Environmetrics Society*, vol. 18, no. 7, pp. 681–695, 2007.
- [31] K. Werner, M. Jansson, and P. Stoica, “On estimation of covariance matrices with Kronecker product structure,” *IEEE Transactions on Signal Processing*, vol. 56, no. 2, pp. 478–491, 2008.
- [32] O. Ledoit and M. Wolf, “A well-conditioned estimator for large-dimensional covariance matrices,” *Journal of Multivariate Analysis*, vol. 88, no. 2, pp. 365–411, 2004.
- [33] Y. Chen, A. Wiesel, Y. C. Eldar, and A. O. Hero, “Shrinkage algorithms for MMSE covariance estimation,” *IEEE Transactions on Signal Processing*, vol. 58, no. 10, pp. 5016–5029, 2010.
- [34] X. Bresson and T. F. Chan, “Fast dual minimization of the vectorial total variation norm and applications to color image processing,” *Inverse Problems & Imaging*, vol. 2, no. 4, p. 455, 2008.
- [35] É. Thiébaud, “Optimization issues in blind deconvolution algorithms,” in *Astronomical Data Analysis II*, vol. 4847. International Society for Optics and Photonics, 2002, pp. 174–183.
- [36] C. Zhu, R. H. Byrd, P. Lu, and J. Nocedal, “Algorithm 778: L-BFGS-B: Fortran subroutines for large-scale bound-constrained optimization,” *ACM Transactions on Mathematical Software*, vol. 23, no. 4, pp. 550–560, 1997.
- [37] P. Delorme, N. Meunier, D. Albert, E. Lagadec, H. L. Coroller, R. Galicher, D. Mouillet, A. Boccaletti, D. Mesa, J.-C. Meunier *et al.*, “The sphere data center: a reference for high contrast imaging processing,” *arXiv preprint arXiv:1712.06948*, 2017.
- [38] R. Galicher, A. Boccaletti, D. Mesa, P. Delorme, R. Gratton, M. Langlois, A.-M. Lagrange, A.-L. Maire, H. Le Coroller, G. Chauvin *et al.*, “Astrometric and photometric accuracies in high contrast imaging: The SPHERE speckle calibration tool (SpeCal),” *Astronomy & Astrophysics*, vol. 615, p. A92, 2018.
- [39] J. Milli, A. Vigan, D. Mouillet, A.-M. Lagrange, J.-C. Augereau, C. Pinte, D. Mawet, H. M. Schmid, A. Boccaletti, L. Matra *et al.*, “Near-infrared scattered light properties of the HR 4796 a dust ring - A measured scattering phase function from 13.6° to 166.6°,” *Astronomy & Astrophysics*, vol. 599, p. A108, 2017.
- [40] A.-L. Maire, T. Stolker, S. Messina, A. Müller, B. A. Biller, T. Currie, C. Dominik, C. A. Grady, A. Boccaletti, M. Bonnefoy *et al.*, “Testing giant planet formation in the transitional disk of SAO 206462 using deep VLT/SPHERE imaging,” *Astronomy & Astrophysics*, vol. 601, p. A134, 2017.

Joint unmixing and deconvolution for angular and spectral differential imaging *supplementary material*

Olivier Flasseur, Loïc Denis, Éric Thiébaud and Maud Langlois

This supplementary material complements Fig.3 of the main manuscript with detailed results about the statistical models of the nuisance component. Figure 1 gives the empirical distribution of the centered and whitened patches (free from object contribution), for different covariance models: diagonal spatial and spectral covariances (i.e., spatial, spectral and temporal weighting) in the first column; full spatial covariance, diagonal spectral covariance, and temporal weighting in second column; full spectral covariance, diagonal spatial covariance, and temporal weighting in third column; and finally the full spatio-spectral separable model introduced in this work (see equation (4) of the main paper) in the last column.

We recall that if random vectors \mathbf{v}_n are accurately modeled by a Gaussian distribution with mean $\boldsymbol{\mu}_n$ and covariance \mathbf{C}_n , then the centered and whitened vectors $\mathbf{C}_n^{-1/2}(\mathbf{v}_n - \boldsymbol{\mu}_n)$ should follow $\mathcal{N}(\mathbf{0}, \mathbf{I})$. Therefore, we compare a standard Gaussian distribution with the empirical marginal distribution of $\mathbf{C}_n^{-1/2}(\mathbf{v}_n - \boldsymbol{\mu}_n)$ for the four models investigated in this paper.

Since the nuisance component is much stronger close to the star (center of the field-of-view), we also compare the empirical distribution of centered and whitened patches located near the host star with patches extracted farther away. The same type of representation was given in Fig.4 of [1] on this dataset for three additional models considered in our previous work for exoplanet detection in angular and spectral differential imaging: (i) no covariance; (ii) only spatial covariances; (iii) spatial covariances plus temporal and spectral weighting.

The full spatio-spectral separable model introduced in this paper appears to be the most accurate to describe statistically the fluctuations of the nuisance component.

Note that, whatever the model, the empirical distribution of the centered and whitened patches follows more closely a Gaussian law with zero mean and unit variance far from the star than near the star, which is to be expected given that nuisances are much stronger close to the star, and spatial as well as spectral correlations are higher (see Fig.2 of the main paper).

References

- [1] O. Flasseur, L. Denis, É. Thiébaud, and M. Langlois, “PACO ASDI: an algorithm for exoplanet detection and characterization in direct imaging with integral field spectrographs,” *Astronomy & Astrophysics*, vol. 637, p. A9, 2020.

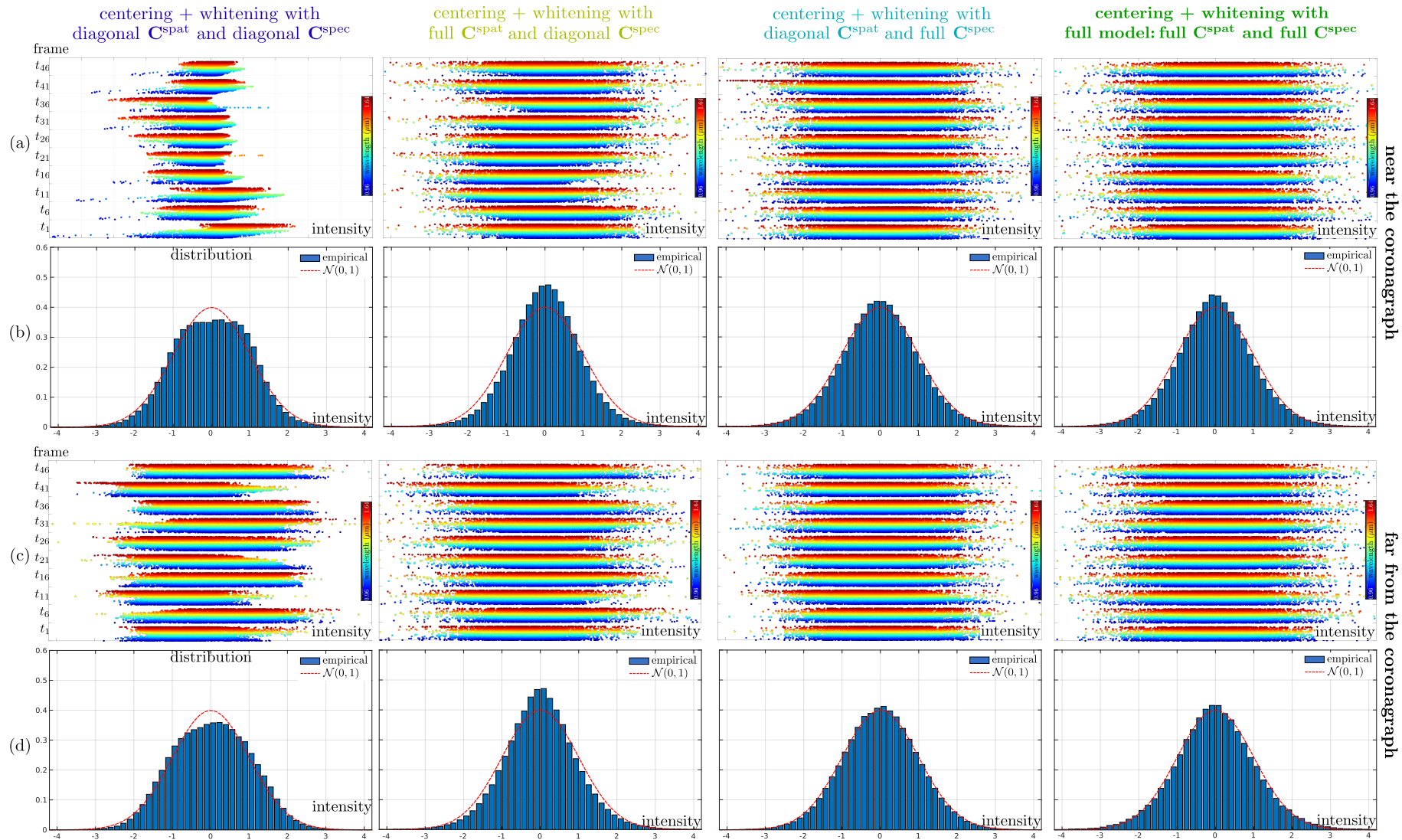


Figure 1: Empirical distribution of the centered and whitened patches: diagonal spatial and spectral covariances in the first column; full spatial covariance, diagonal spectral covariance, and temporal weighting in the second column; full spectral covariance, diagonal spatial covariance, and temporal weighting in the third column; and finally in the last column the full spatio-spectral separable model introduced in this work. Rows a and b: location selected at a small angular separation; rows c and d: location at a larger angular separation. The empirical distribution computed over the whole field of view is given in Fig.3 of the main paper. Patches represented in this figure contain only the contribution from the nuisance component (i.e., no exoplanet or disk).